LAWRENCE
LIVERMORE
NATIONAL
LABORATORY

Compact Torus Accelerator Driven Inertial Confinement Fusion Power Plant HYLIFE-CT

B.G. Logan, R. W. Moir, M. Tabak, R. L. Bieri, J. H. Hammer, C. W. Hartman, R. L. Leber, R. W. Petzoldt, M. T. Tobin, M. A. Hoffman

April 1, 2005

Disclaimer

Compact torus accelerator driven
inertial confinement fusion power plant
HYLIFE-CT*

B. G. Logan, R. W. Moir, M. Tabak, R. L. Bieri, J. H. Hammer, C. W. Hartman, M. A. Hoffman, R. L. Leber, R. W. Petzoldt, and M. T. Tobin

February 15, 2005

ABSTRACT

A Compact Torus Accelerator (CTA) is used to accelerate a Compact Torus CT) to 35 MJ kinetic energy which is focused to a 20 mm diameter where its kinetic energy is converted to a shaped x-ray pulse of 30 MJ. The capsule yield with a prescribed radiation profile is calculated to be (gain 60 times 30 MJ) 1.8 GJ. Schemes for achieving this profile are described. The CT is accelerated in a length of 30 m within an annulus of 150 mm ID and 300 mm OD where the maximum magnetic field is 28 T. A 2.5 m conical taper reduces the mean diameter of the CT from 225 mm to 20 mm. The conical section is made out of solid Li_2BeF_4. The target with its frozen conical guide section is accurately placed at the end of the accelerator about once per second. The reactor called HYLIFE uses liquid jets to attenuate blast effects including shrapnel from the shattered conical guide section and radiation so that the vessel is expected to last 30 years. The calculated cost of electricity is estimated (in constant 1988 dollars) to be about 4.8 ¢/kW·h compared to the future cost of nuclear and coal of 4.3 to 5.8 ¢/kW·h. The CT driver contributes 17% to the cost of electricity. Present CT's make 2×10^8 W/cm^2; the goal of experiments in progress is 10^{11} W/cm^2 with further modifications to allow 10^{12}W/cm^2, whereas the reactor requires 10^{15} W/cm^2 in a shaped pulse.

This page intentionally left blank.

This page intentionally left blank.

Table of Contents

This page intentionally left blank.

The CT is made in a magnetized coaxial gun of 2-m mean diameter as shown in Fig. 1–1. After a 3-m long conical compression section, acceleration takes place over 27 m. In the final 2.5 m, focusing takes place where the 225 mm dia CT is focused to 20 mm. The accelerator, positioned vertically, injects the CT into the reactor. The accelerator, reactor and target injection systems are shown if Fig. 1–2. Each of these components will be described in the following section. In the accelerator the maximum magnetic field on the walls, which are assumed to be copper–lined steel, is 28 T. The pressure and thermal pulse on the walls as the CT goes by is assumed to result in a low enough stress so that fatigue lifetime will be long. In the 2.5 m long conical section however the field and, hence, pressure quickly rises so that fatigue and shock rupture will limit the lifetime. This last 2.5 m section is designed to be destroyed on each shot, but will survive till the CT has reached the target.

The reactor vessel is shown in Fig. 1–3. Streams of falling molten salt jets just as in HYLIFE–II (Moir, 1991) absorb the neutrons, breed tritium, and attenuate the shock so the walls see a mild pressure pulse.

The target assembly mechanisms discussed later insert the final focus section and target on each shot. This final focus section is made of cast salt – a glass or crystaline-like material shown in Fig. 1–4.

The rapidly changing magnetic field at the leading edge of the CT causes surface breakdown and plasma formation so that Li_2BeF_4 guide material should result in little field penetration and therefore good guidance of the CT with little slowing down. If necessary, a metallic coating $\simeq 10\ \mu m$ thick can be added to the cone surface to improve conductivity. As the CT coasts down the conical section it is compressed and enter the trapping region shown in Fig. 1–5. The CT enters through a 2 mm annulus and shock heats when the CT hits the end of the target. Much of the CT kinetic energy is converted into internal energy (temperature).
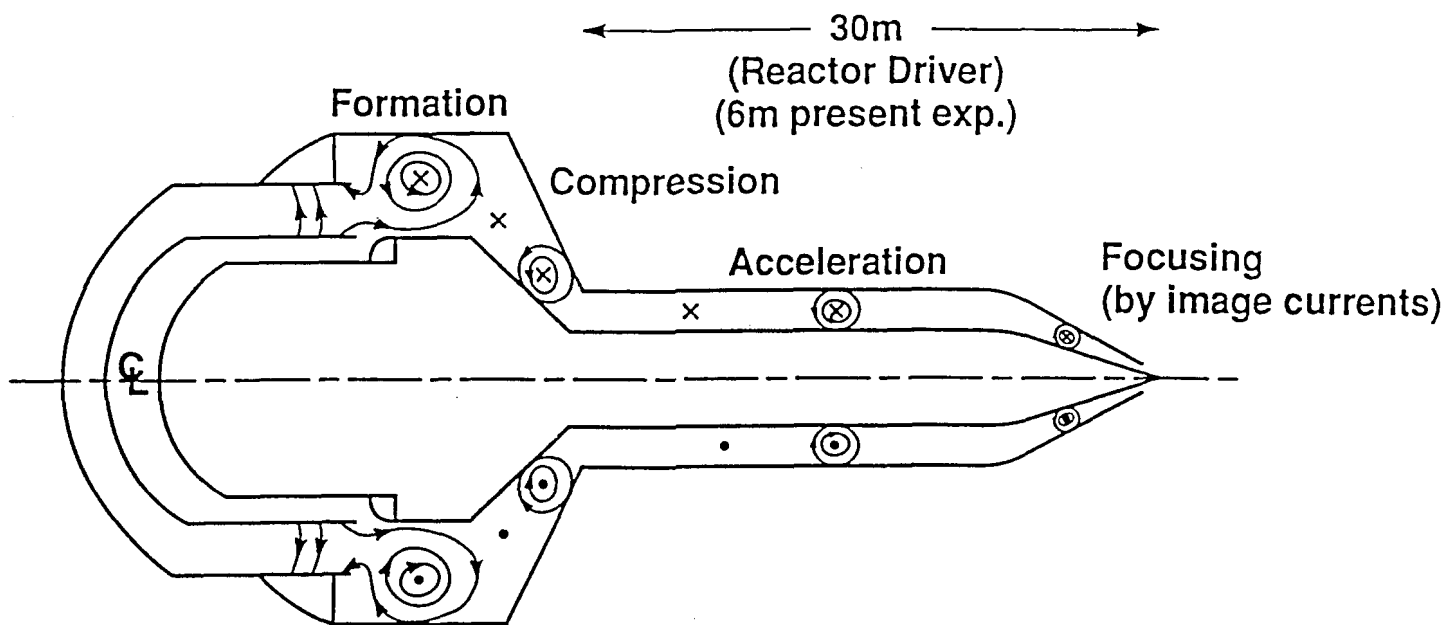
02-15-0490-1984

- The compact torus is stable, requires no external coils for equilibrium, and has a long lifetime
- The accelerator operates as a coaxial rail gun with the compact torus as the armature
- Acceleration to large directed kinetic energy ($\approx$40 MJ) and velocities of 10^8–10^9 cm/s are predicted with focusing to high power density (10^{16} W/cm^3) at $\approx$ cm dimensions
- The torus energy can be efficiently converted to soft xrays at the target

Fig. 1-1. The compact torus accelerator is based on $\vec{J} \times \vec{B}$ acceleration of charge-neutral magnetically–confined plasma rings.
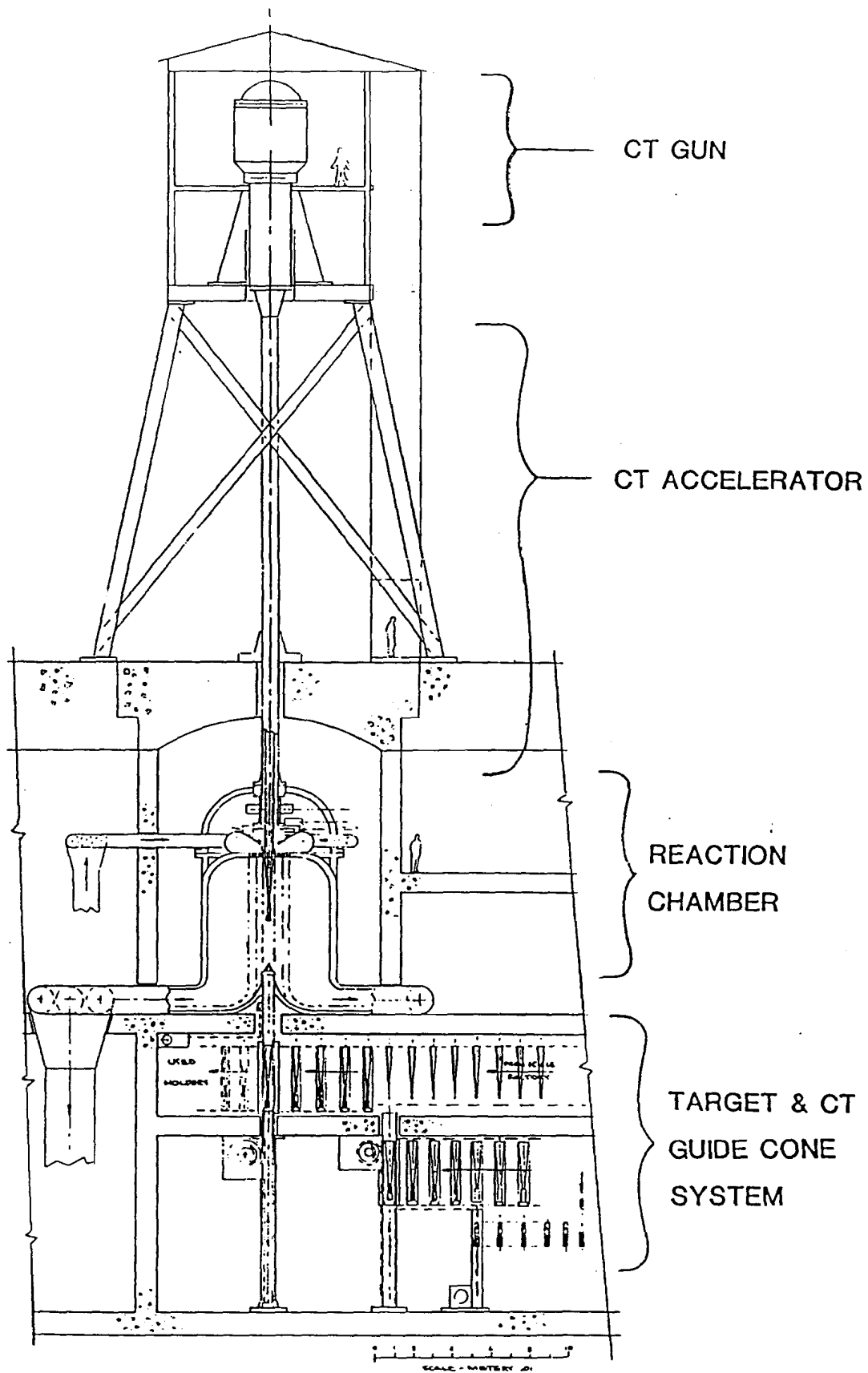
Fig. 1–2. CT reactor including the accelerator, reactor chamber and final transport/
target insertion system.
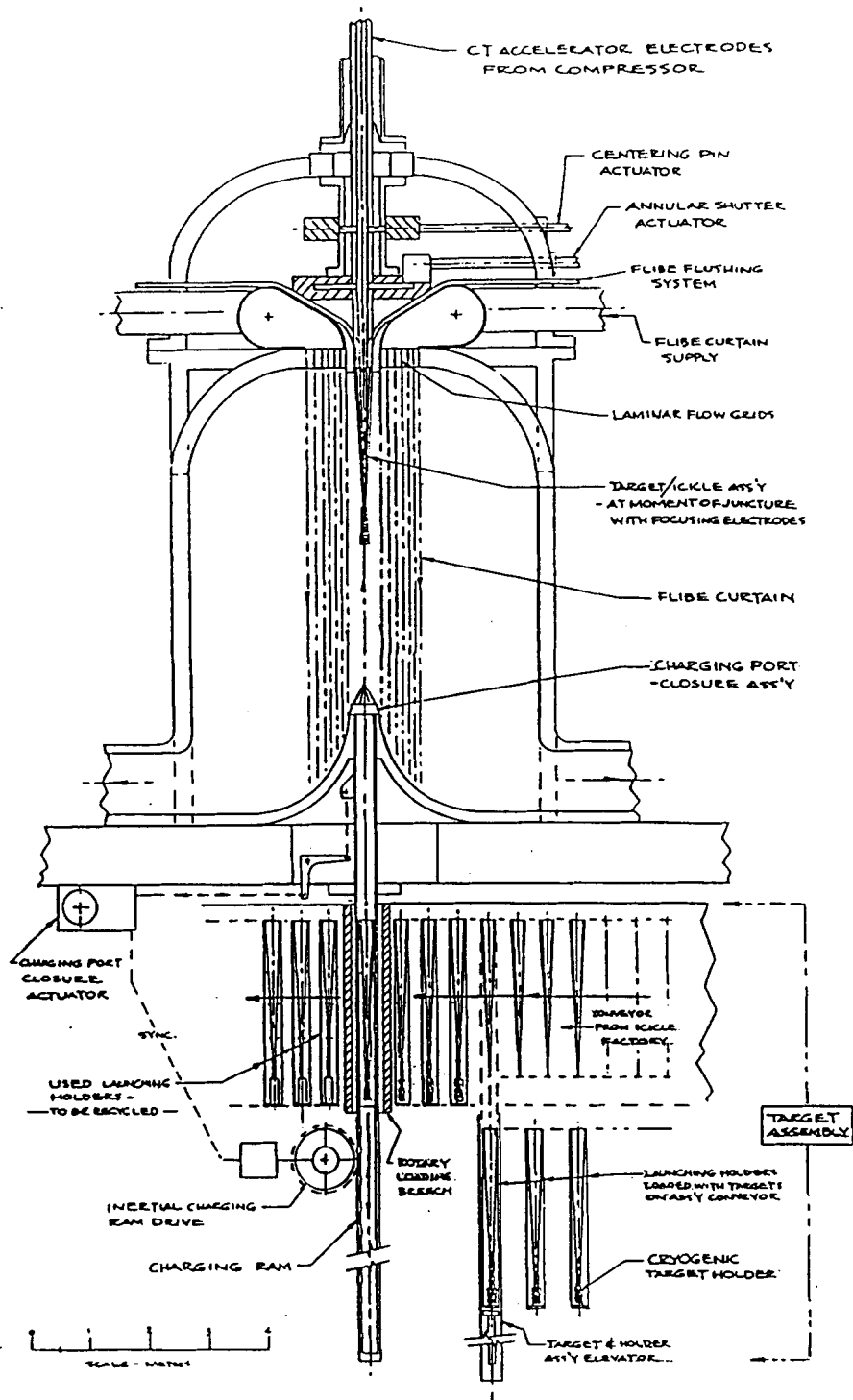
REACTION CHAMBER AND TARGET ASSEMBLY

Fig. 1–3. Streams of falling jets of molten salt absorb the neutrons, breeds tritium, and attenuate the shock so the wall sees a mild pressure pulse. The debris from the shattered frozen salt guide section is also stopped by the molten salt jets.

10

OD=300 mm

ID=150 mm

r=225 mm

$B = 28 \ T \propto \triangle^{-1} \ r^{-1}$

$\triangle = 75$ mm

1 M

X—X
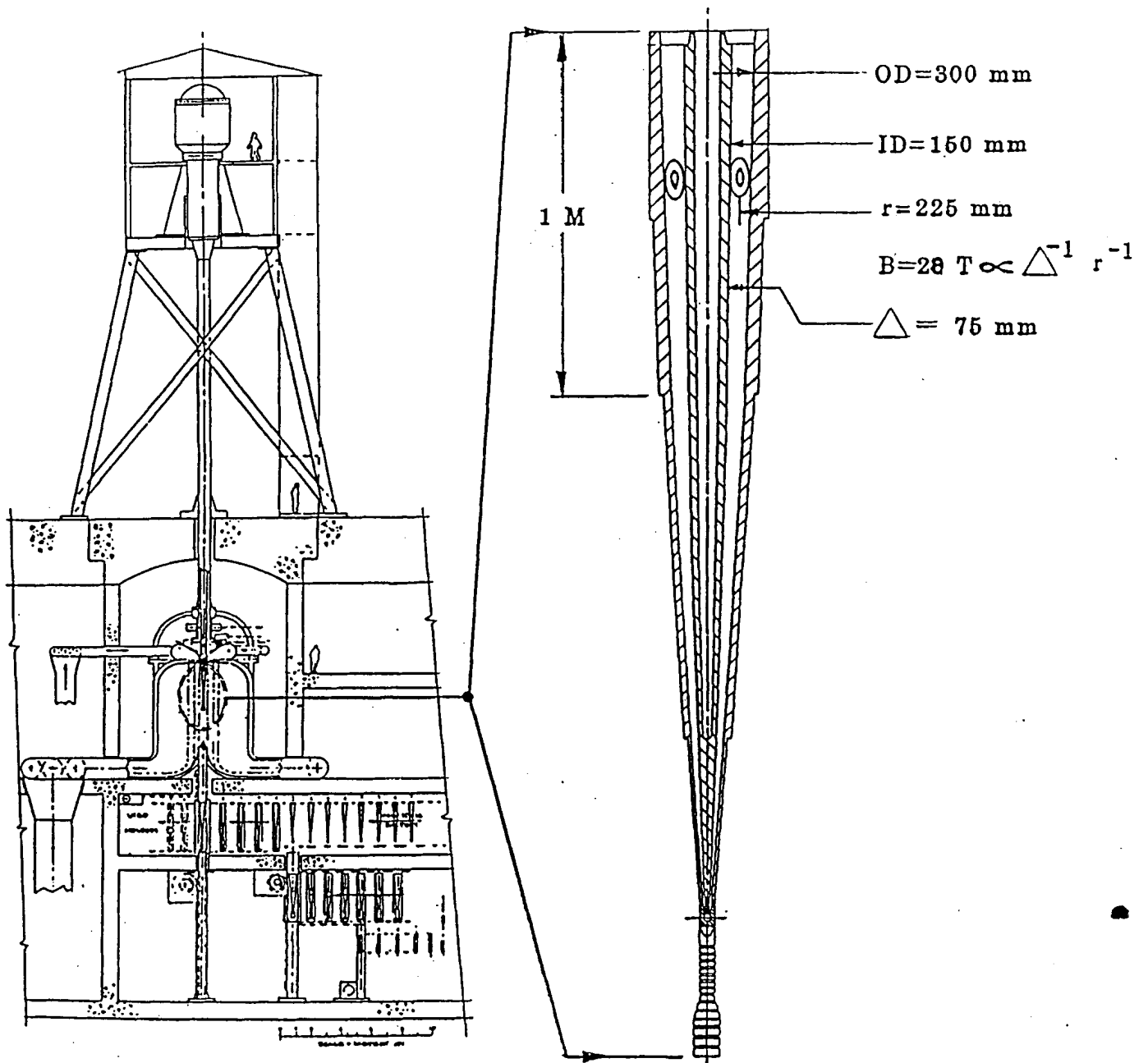
Fig. 1–4. CT final transport system. The 2.5 m long focus section guides the CT to a diameter of 20 mm at the target. It is made of fozen Li_2BeF_4 and shatters after each shot.

Li or
Li_2BeF_4
protects
accelerator
from neutrons

$\Delta = 2$ mm

0 2 4 6 8 10 12 mm

Small enough gap so
CT will enter but not
rebound and not leak
too much radiation

40 cm

Frangible tailpiece
and
target sleeve
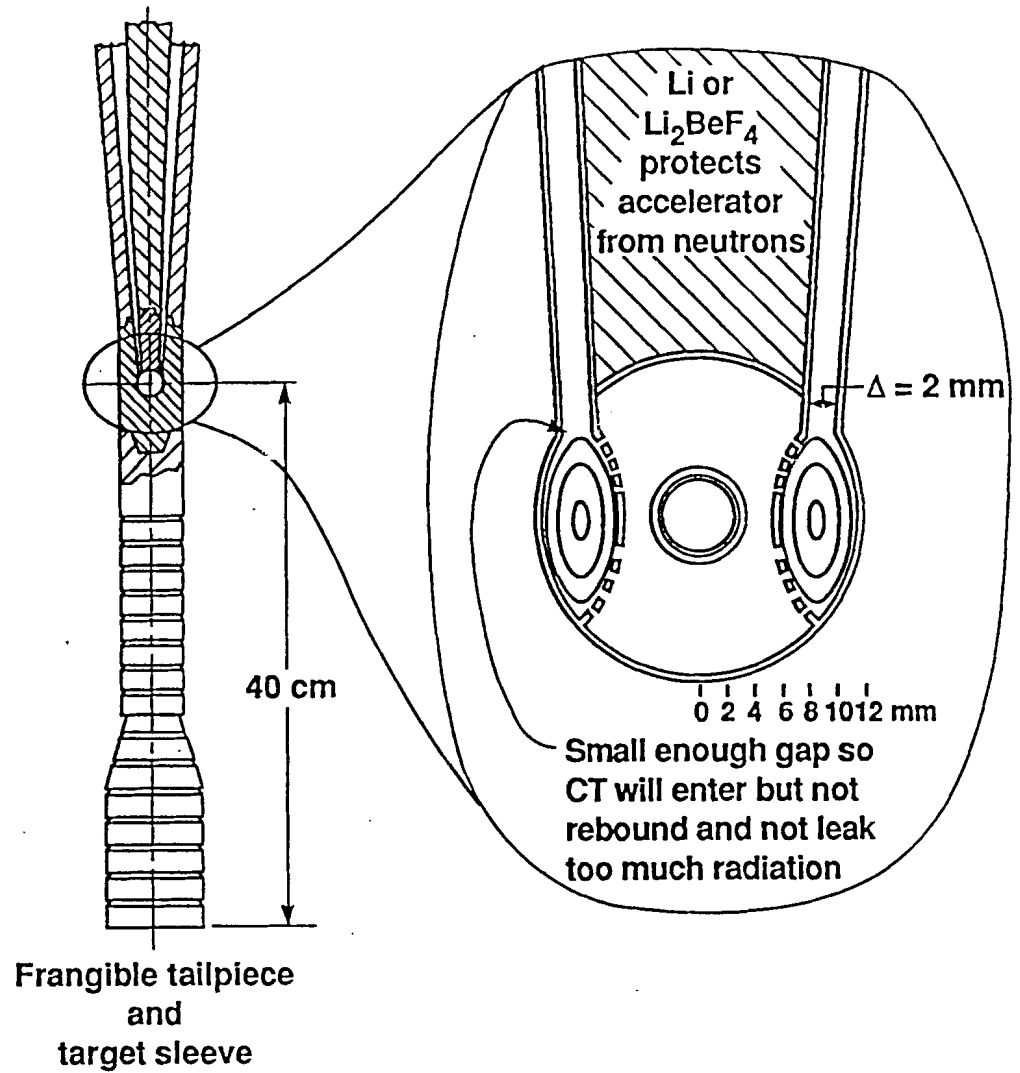
Fig. 1–5. The CT is transported, focussed, and delivers 30 MJ of x rays to the target region shown in the figure.

Magnetic tension thus prevents the CT from bouncing back out the annulus (i.e., the CT is trapped). The CT undergoes a radiation collapse where its 40 MJ of energy are converted into 30 MJ of x rays, that enter the hohlraum and drives the capsule, which is discussed in Chapter 2, "Target Design and Performance." The x rays fill the hohlraum by passing through holes in the high-Z region shown in Fig. 1-5. The mass of the high-Z material prevents premature collapse onto the capsule. The yield of the capsule is calculated to be 1.8 GJ from the 36 MJ CT.

The target assembly mechanism shown in the bottom of Fig. 1-3 performs several tasks. The cryogenic capsule is inserted into the hohlraum and its cryogenic holder, which is about 100 mm tall, is shown in Fig. 1-5. A frangible tailpiece is attached below, whose purpose is to attenuate neutrons and thus protect the mechanisms below the target from blast and neutrons. The target is attached to the warm 2.5 m long guide section (Fig. 1-4). A holder surrounds and supports the guide or focusing section (Fig. 1-6). The holder translates horizontally to a position directly below the reactor chamber. Then the holder is inserted upward and quickly brought back down. A charging port closure assembly is then closed (see Fig. 1-7). The cast salt focusing section continues moving upward toward the bottom of the accelerator.

Just at the moment the focusing section almost touches the solid part, the CT is fired (formed, accelerated, and focused). The critical dimensions are those at this "touching" point. The CT would shock heat itself if it ran into a "bump" while making the transition which would limit the ability of the CT to focus onto the target. Clearly the feasibility of the concept depends on a smooth transition and needs study and experimental confirmation.

The solid guide section will either shatter into small pieces or be turned into liquid and vapor by the CT and capsule energy release. The 0.4 m or more of material directly above the capsule will strongly attenuate line-of-sight neutrons and solid debris from going up the beam line. A fraction of second bounce

FLIBE ICICLE ENTERING

LAUNCHING HOLDER

RETRIEVABLE

LOW-MASS

LAUNCHING HOLDER

ASSEMBLED UNIT

READY FOR LAUNCHING

OR

CRYOGENIC STORAGE

TARGET ENCASED IN
CRYOGENIC SABOT

FRANGIBLE
FLIBE TAILPIECE
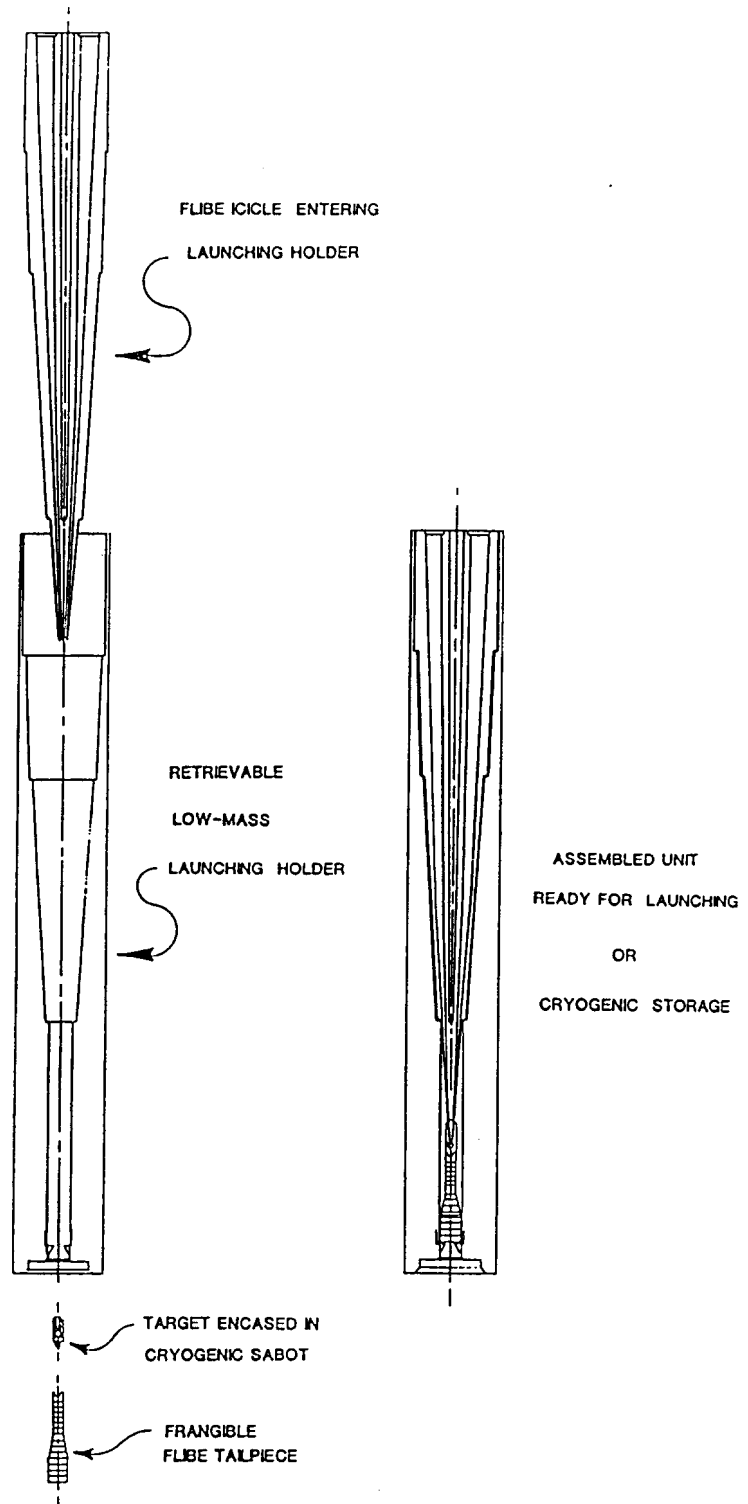
Fig. 1–6. The coaxial frozen salt guide section and target encased in its cryogenic
sabot are shown being assembled in the assembly unit.

14
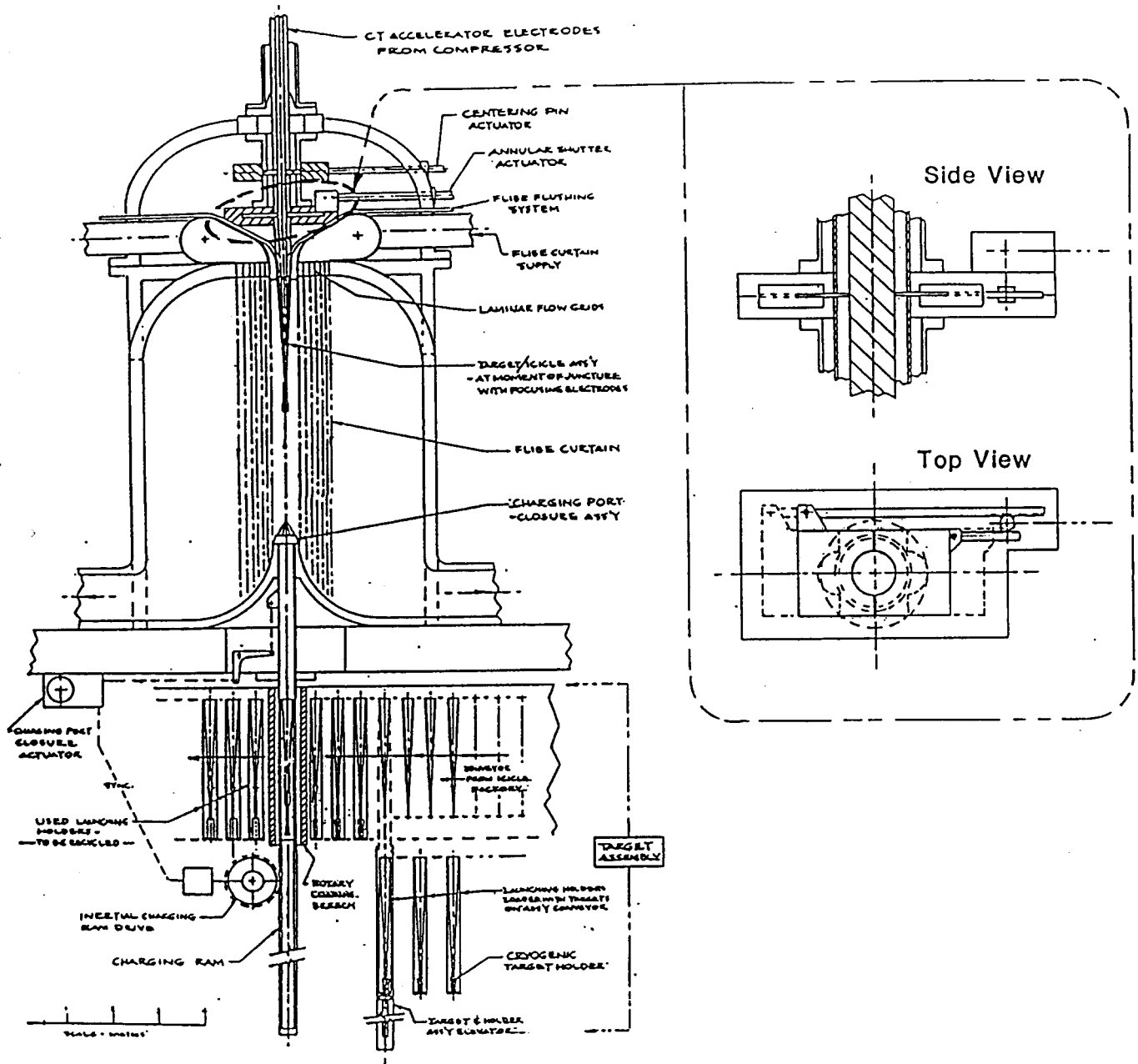
Fig. 1–7. A fast shutter closes off the accelerator from the reactor chamber preventing liquid and salt vapor from contaminating the accelerator.

15

neutrons, however, will go up the beam line. Vapor and liquid in some amount will also go up the beam line and freeze out on the accelerator surfaces requiring periodic removal by heating up above the melting point (460°C for Flibe and 190°C for Li). To avoid too much vapor and liquid being ejected up the beam lines, we employ a fast shutter as in many ICF power plant designs. A shutter is shown in Fig. 1–7. The walls below the shutter could be kept just above the melting point of Flibe (460°C) to prevent buildup of frozen salt.

As the CT passes, shock waves shatter the thin walled guide tube (made of $\approx$ 1 mm glass-like solid Li_2BeF_4 wall). The new guide tube would have to be put in place in about 0.7 sec for a 1.5 Hz repetition rate. The center coaxial tube is unsupported except at the bottom. Centering fingers at the top will be needed that are withdrawn just before the CT passes. The approximate mass of this 2.5m long guide tube is 3 kg of Li_2BeF_4. The liquid jets of the HYLIFE will attenuate blast and radiation so that neutron damage to the wall is reduced giving the wall a 30–year lifetime.

The liquid jets (Li_2BeF_4 or Li) will breed tritium and carry the heat produced to the balance of the power plant which is of more or less conventional design ($NaBF_4$ nonradioactive intermediate coolant and a steam generator and turbine system).

References

R. W. Moir (1991), "HYLIFE-II Inertial Confinement Fusion Reactor Design," *Fusion Technology,* **19** 617 (1991).

2.0 Target Design

In the following section we discuss target design and performance with an assumed pulse shape, we then discuss tailoring the CT profile to achieve the desired pulse shape and finally discuss uncertainties.

2.1 Target Design and Performance

Figure 2.1–1 shows a schematic cross–section of an ICF target driven by a single compact torus of 40 MJ (32 MJ kinetic +8 MJ magnetic energy). This concept assumes pulse–shaping can be achieved by proper tailoring of plasma density, impurity, and magnetic flux profiles in the incoming CT, allowing single CTA pulses to drive the target through a single reactor port (cone) as described in Section 1.0. Pulse-shaping achieved by a natural radiative collapse of the CT's magnetized boundary layer would add the least complication to the target physical design, and was chosen as the basis for this design. However, pulse–shaping could also be obtained by introducing either small spherical high–Z pellets or by impaling the CT on long high–Z spikes (bed–of–nails). These approaches await future work. More complicated reactor / target schemes could also be considered using a CT without pulse shaping in combination with a laser or heavy–ion beam supplying a pre–pulse energy of about 1 MJ. The first step in this design concept was to use LASNEX to find a minimally adequate soft x–ray pulse shape to get a minimally-sufficient capsule gain. The input CT energy of 40 MJ is chosen simply because it was the largest CT energy for which an existing CTA bank design and cost was available (100 MJ bank, see Section 3.0). Given a RACE accelerator efficiency of 40 to 50%, we ran LASNEX looking for a minimal capsule yield in the range of 2 GJ. Such a yield could be accommodated in a HYLIFE reactor vessel of about 5 m radius, and would give a reasonable ηG product ≥ 20 for a commercial reactor. After determining an acceptable soft x–ray pulse to achieve this,
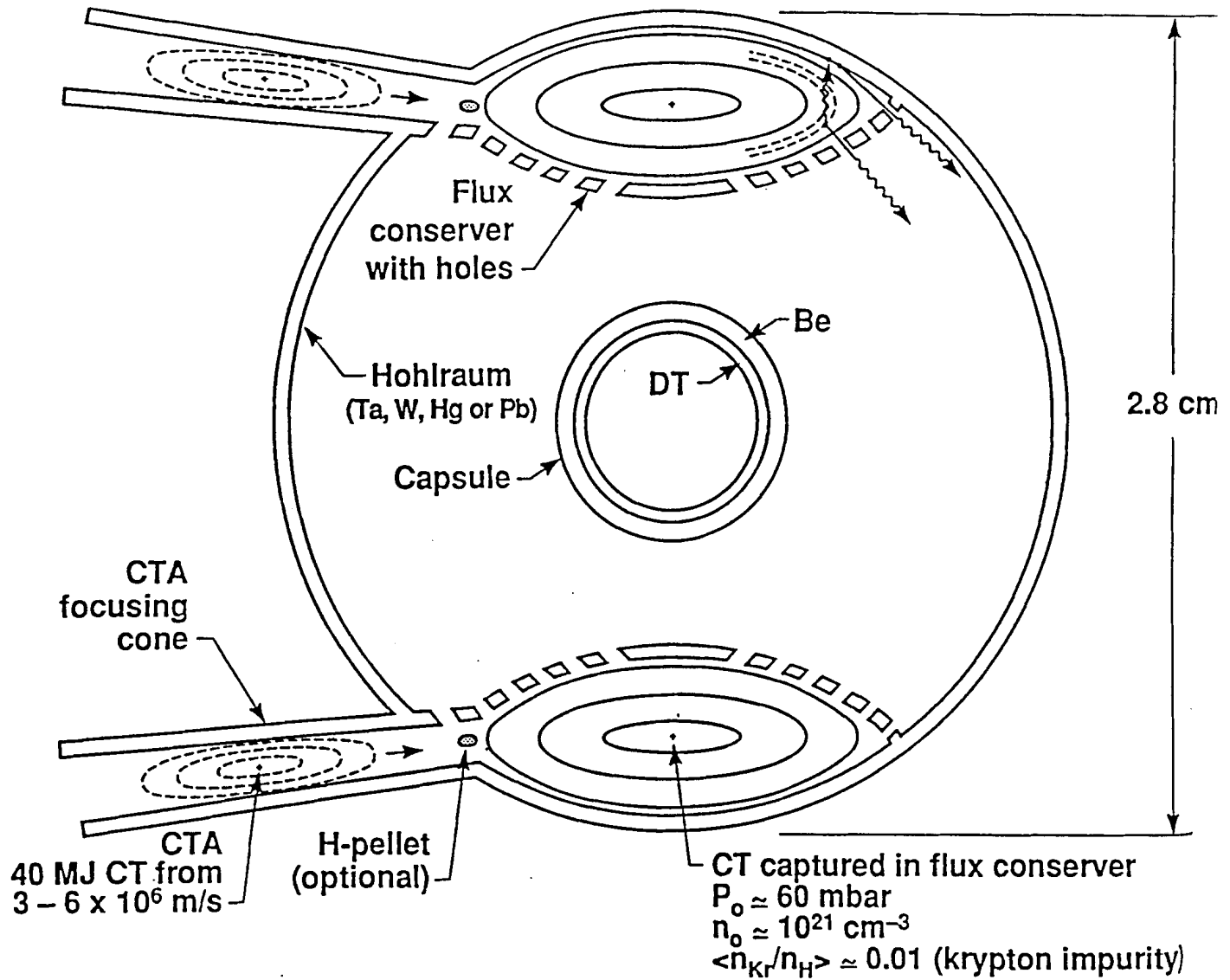
Fig. 2.1-1. RACE indirect–drive ICF target. The dimensions of the flux conserver with hole has not been determined.

using LASNEX, the required CT profiles are then determined to reproduce such an x-ray pulse as closely as possible.

In Fig. 2.1-1, a CT from the CTA is focused down an annular cone and enters the flux-conserver compartment from an annular entrance slot shown on the left. The density profile within the CT may be modified as needed by addition of cryogenic hydrogen pellets as indicated near the entrance. The CT crosses the flux conserver cavity in about 5 nsec, and generates a strong shock from encountering the far end of the cavity, which converts the CT's initially directed kinetic energy into thermal plasma pressure. TRAC[4] calculations show that the CT expands to fill the flux conserver cavity, whose size is adjusted with respect to the entrance slot cross section so that the resultant plasma pressure is too low to overcome magnetic tension forces that would arise in re-expansion through the entrance slot. Thus, the nonadiabatic shock heating results in capturing the CT in the flux conserver. At the densities (predominantly hydrogen plasma) chosen in this example, the ion-electron equilibration time is fast enough so that T_e rises to about 16 KeV after the first Alfvèn time (5 nsec) after capture. The magnetic diffusion skin time under these conditions much exceeds the inertial confinement time due to the mass of the flux conserver walls, so that the magnetic flux (ψ) gets compressed like a sandwich between the conductive hot plasma and the flux conserver (see Fig. 2.1-2) and thus prevents hot plasma flow back out the entrance hole and other small holes (for radiation) in the inner flux conserver (barrier). The CT remains in the MHD limit since the gyro-orbit of ions is small compared to the hohlraum dimensions. A key issue is the MHD stability of the magnetic flux layer. LASNEX calculations by Jim Hammer have shown 2-D (r-z) stability for 10-20 ns for $U_k/U_m \approx 3$, but more calculations are needed to see if stability persists at the higher $U_k/U_m \approx 5$ in this example. If the stability limit were restricted to $U_k/U_m < 3$, more magnetic flux and magnetic energy would be needed, raising the total input CT energy and lowering the fusion gain correspondingly. Assuming

Density at exit of cone

Density in flux conserver X50

Field pressure at cone exit

Field pressure in flux conserver

Density n (10^{28} m^{-3})

Field pressure $\dfrac{B^2}{2\mu_o}$ (Mbar)

CT minor radius (normalized) $\dfrac{r}{a}$
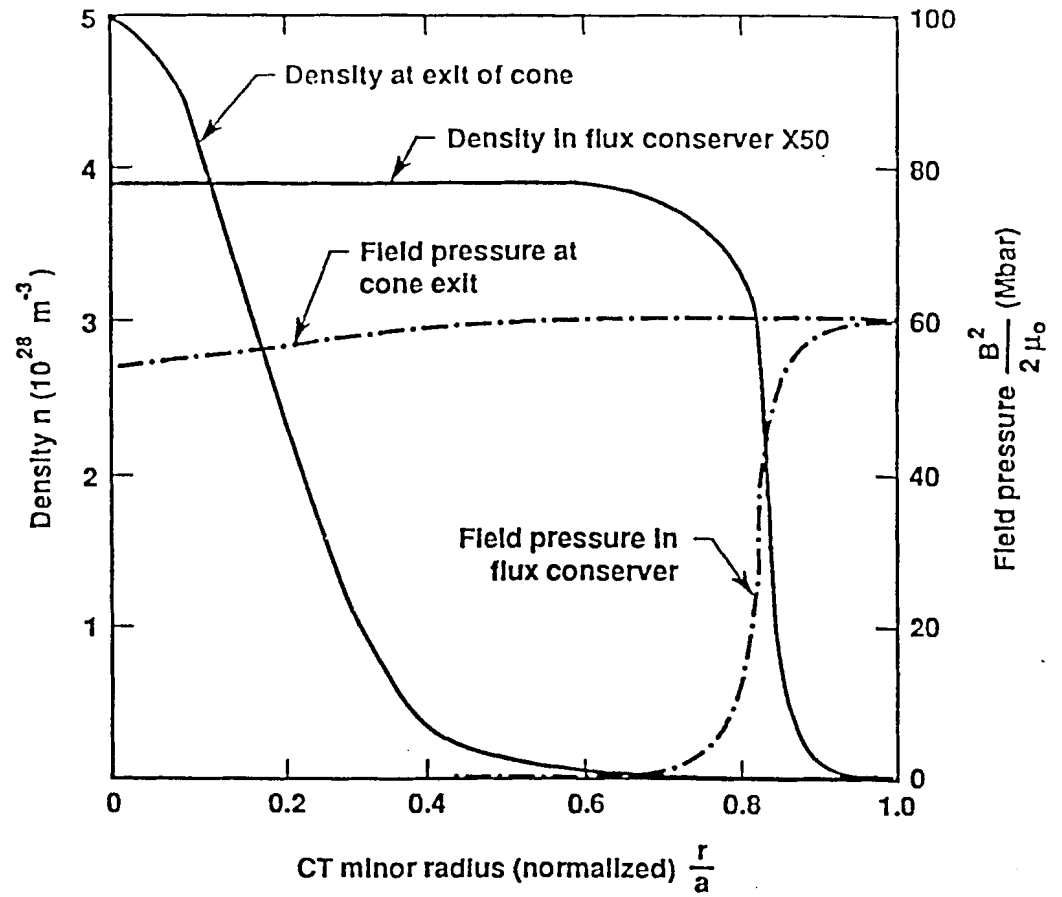
a_{CT} = 2.66 mm in flux conserver
a_{CT} = 0.67 mm at cone exit
$n/n_o = (1-\psi/\psi_m)^{\alpha_n}, \alpha_n = 15$
n/B = const. mapping
$U_k/U_m = 5$

Fig. 2.1-2. CT density and field pressure versus normalized minor radius r/a, at cone exit (entrance to flux conserver) and after pressure equilibration (point A) inside flux conserver.

stability, the CT enters the hohlraum, stagnates and then couples its internal energy to the high–Z wall over a 50 ns time period. The CT maintains its magnetic field during this period. The magnetic field applies a pressure of >60 Mbar to the hohlraum walls during this time. This pressure, which could, without a barrier, lean on the capsule asymmetrically, requires a conductive wall (with holes to transmit x–rays) and enough mass to contain the CT pressure inertially for 50 ns.

A satisfactory solution uses a high–Z, high mass barrier. The heat capacity of this barrier is limited to the thin layer covered by the Marshak wave. The average thickness / mass per unit area must allow for holes in this barrier to allow radiation to reach the capsule. With sufficient flux layer thickness, the CT will not escape through holes smaller than approximately 1 mm. We envision a thick metal barrier pierced with 1 mm diameter holes whose total area covers 2π steradians. A particularly useful high-Z material is Ta because it is soluble in Flibe and is easily recovered.

Figure 2.1–3 is a pie diagram showing the capsule design, including barrier and hohlraum. The LASNEX problem was run with a leak source in the outer chamber, which was to mock up the energy lost to the capsule and the CT entrance hole. The CT was modeled with pressure sources pushing the barrier and hohlraum wall and with a laser source depositing energy into the hohlraum wall. The x ray source energy supplied by the CT was 28 MJ and the capsule yield was 1.8 GJ. Figure 2.1–4 shows the pulse shape assumed for the delivery of energy from the CT to the wall of the hohlraum. Figure 2.1–5 shows the radiation temperature in the outer channel and the radiation temperature driving the capsule. The radiation temperature driving the capsule is consistent with half the flux in the outer hohlraum. Figure 2.1–6 shows the energy absorbed by the capsule together with the energy leaked through our artificial "hole." Our energetics are about right, with slightly more energy lost by the outer channel than is absorbed by the capsule. Realistic CT entrance ports may allow more escaped energy than assumed
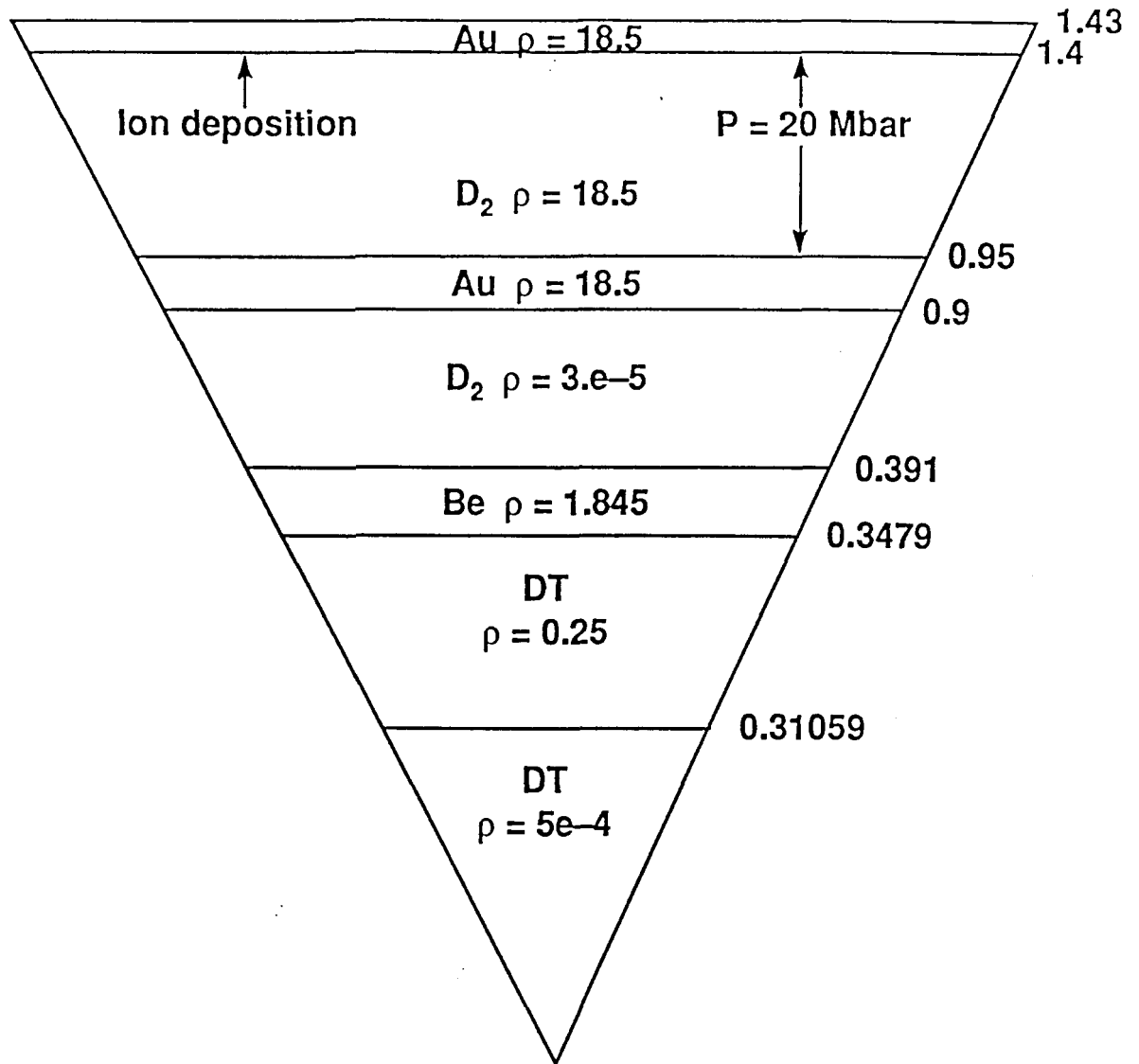
Fig. 2.1–3. One-dimensional pie diagram of implosion capsule together with hohlraum enclosing it.
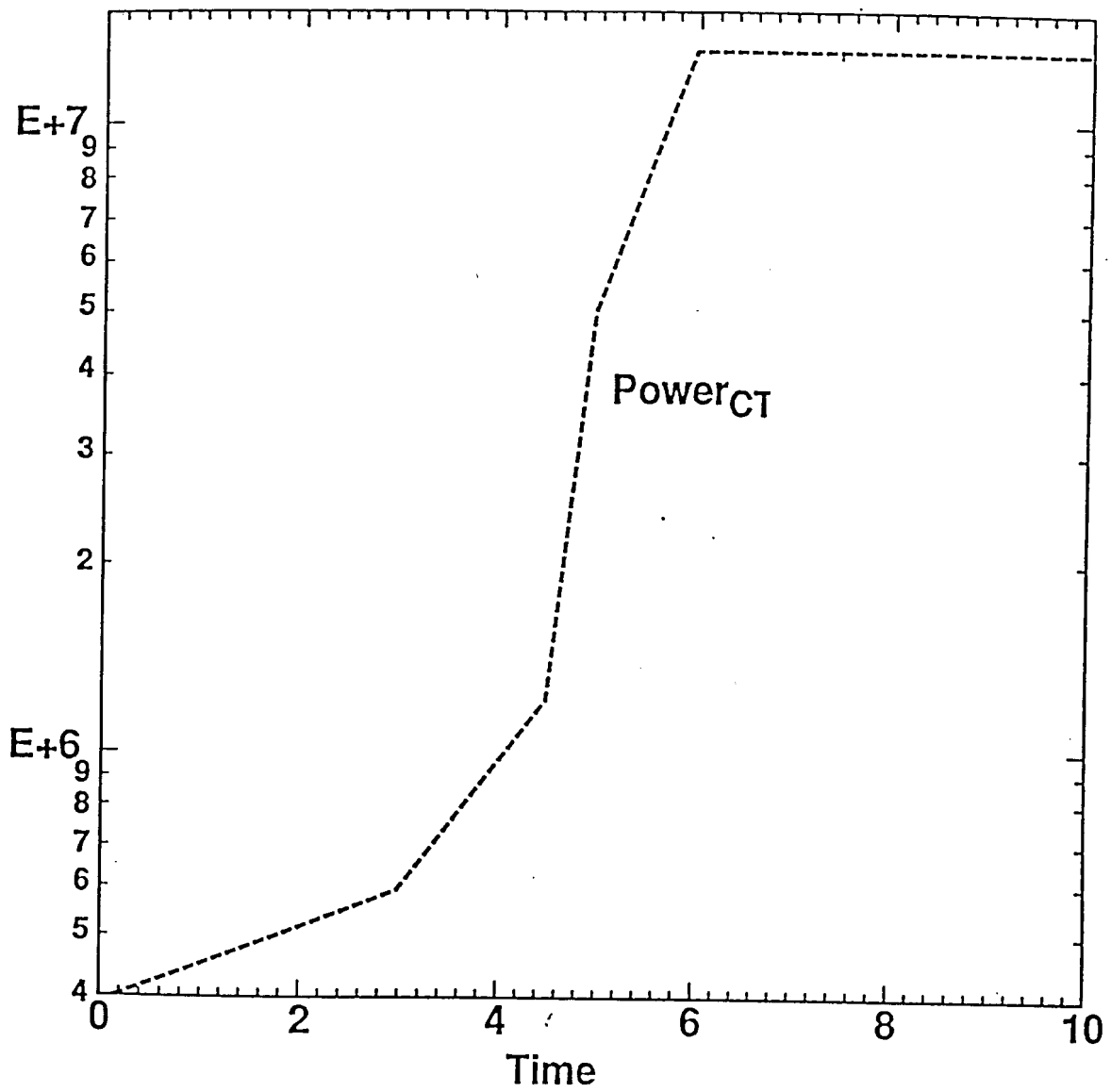
Fig. 2.1–4. Radiation power supplied to capsule–hohlraum system.
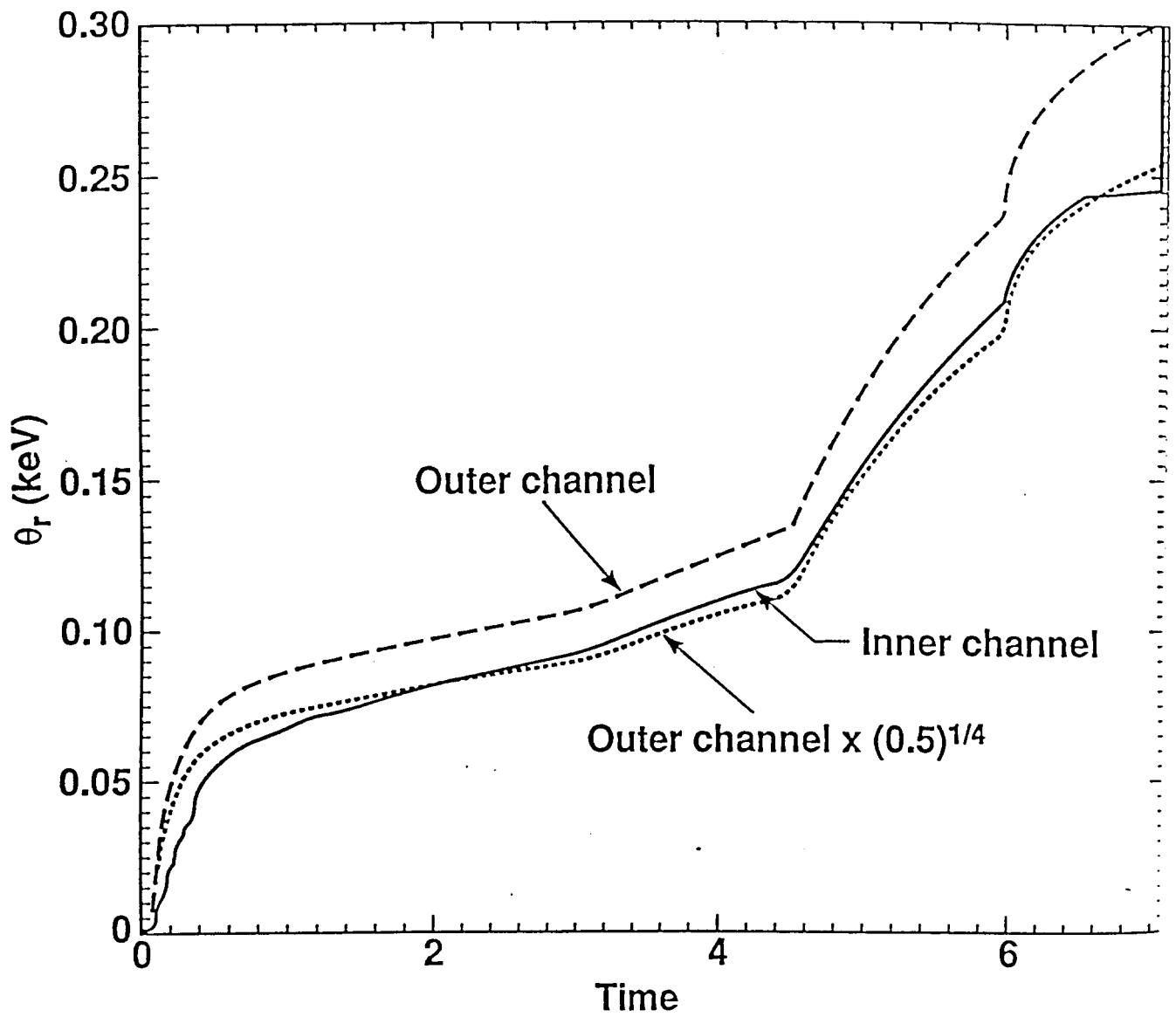
Fig. 2.1–5. Radiation temperatures in inner and outer hohlraums.
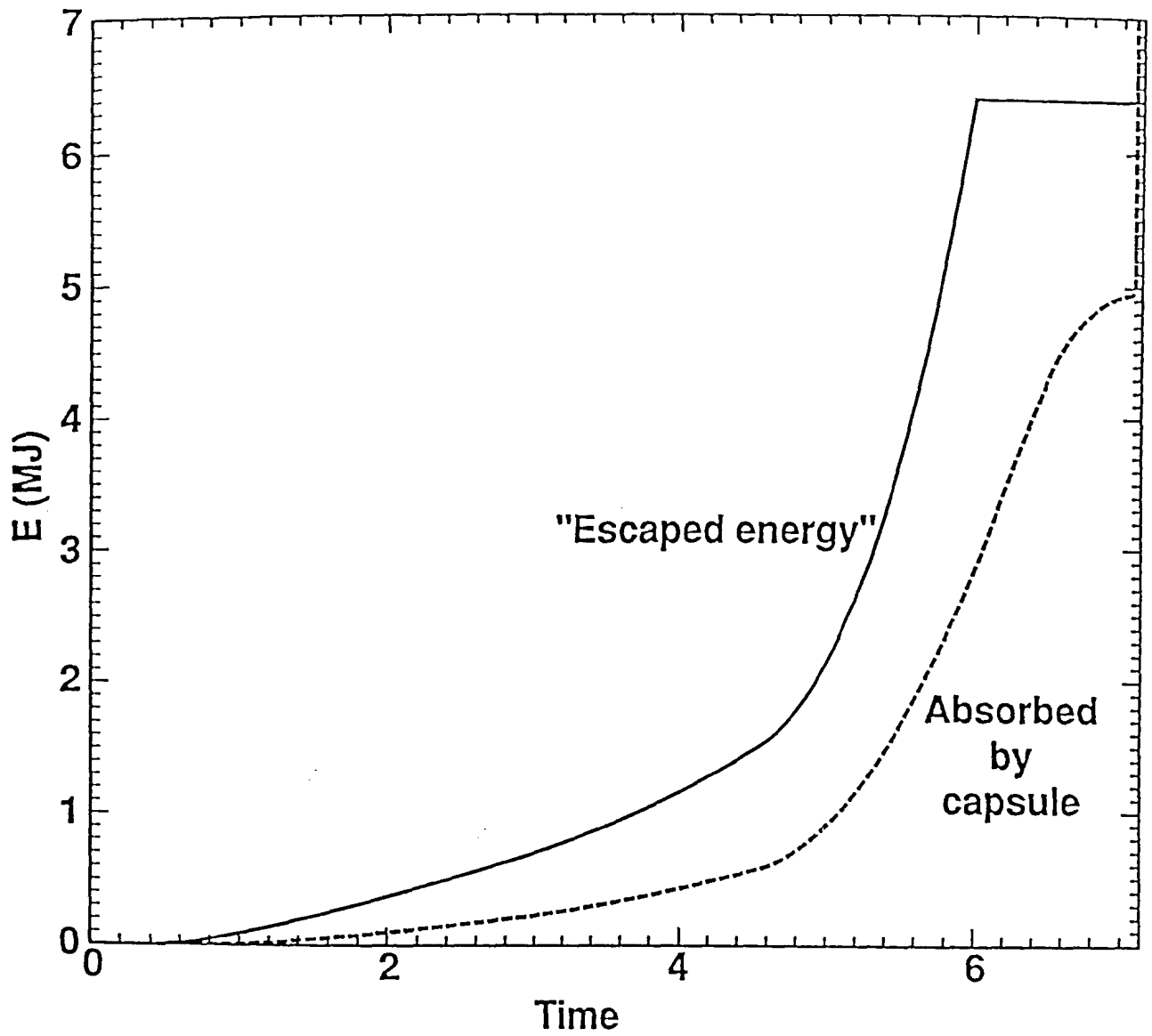
Fig. 2.1–6. Energy lost through artificial leak compared with that absorbed by capsule.

in this LASNEX model, but the error is not large. The energy lost to the barrier is slightly overestimated. The radiation temperature in the outer channel is affected by the energy loss into the barrier. In the 1–D problem this is given by one side of a 4π barrier heated at the outer channel temperature, while the real problem would have a 2π barrier heated on two sides at slightly different temperatures. Figure 2.1–7 shows that the barrier does not collapse upon the capsule during the implosion time. The effective case to capsule radius ratio is not greater than at the symmetry plane of a laser–driven LMF design. This CT design would be about as sensitive to sonic reflections from the high–Z barrier as is a laser hohlraum.
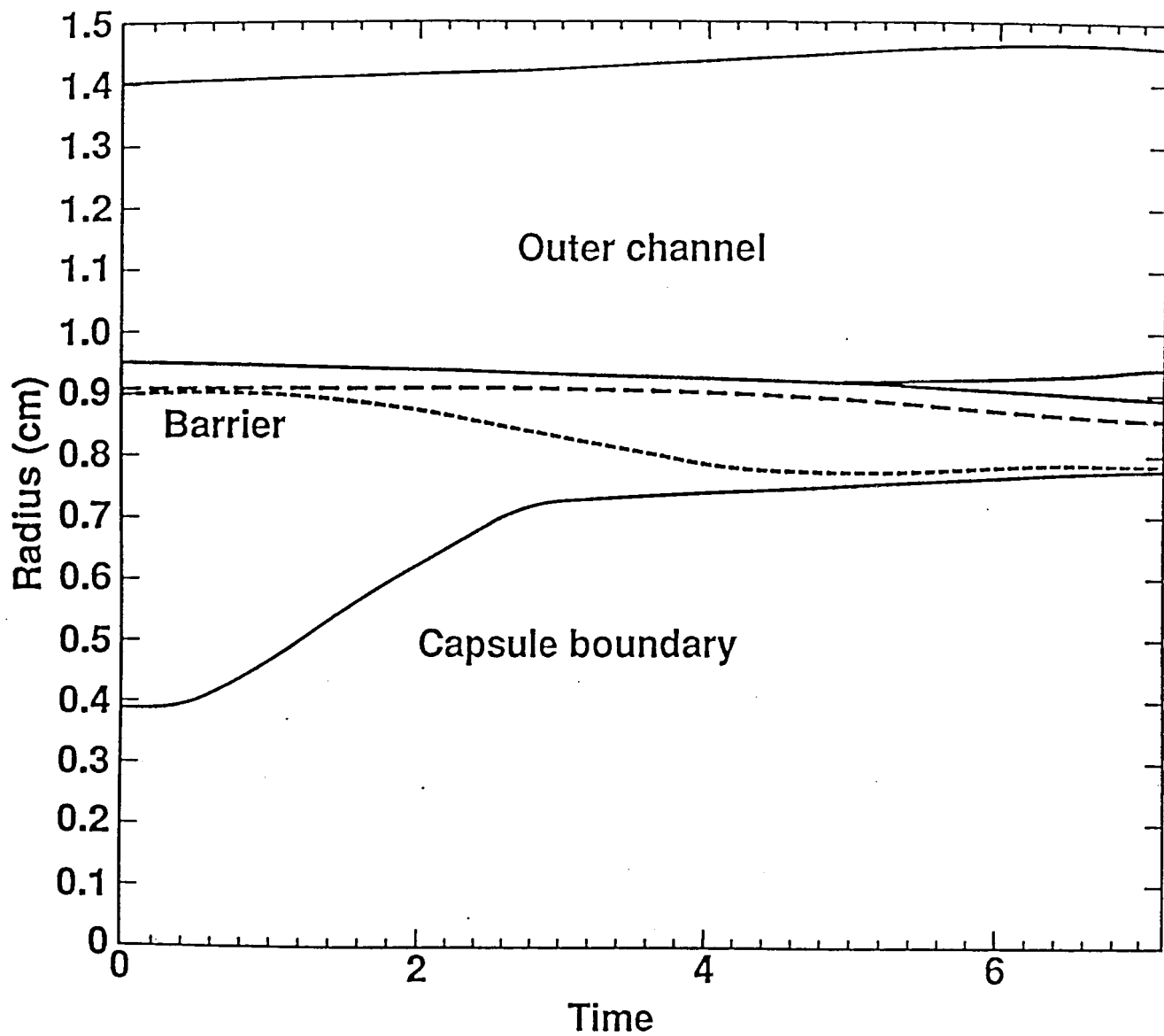
Fig. 2.1–7. Positions of boundaries of channels and capsules. Magnetic pressure in
outer hohlraum keeps high–Z walls from blowing in.

2.2 Tailoring CT Profiles to Achieve the Desired Pulse Shape

The basic approach proposed for pulse shaping is to seed the edges of the predominantly hydrogen hot plasma with a few percent of moderate to high–Z impurity (such as krypton, whose radiation per ion per electron vs. Te is shown in Fig. 2.2–1), and, given proper initial radial profiles of hydrogen plasma, impurity concentration, and magnetic field, allow the captured CT to radiatively decay from its impurity radiation (optically–thin radiation from the CT plasma volume). The desired pulse shape is controlled by four factors: (1) the variation of optically–thin radiation rate with temperature to a chosen impurity species such as krypton (Fig. 2.2–1), (2) the U_k/U_m ratio of the CT injected into the flux conserver, which controls the relative plasma and field pressures within the CT, (3) the distribution of plasma density with CT magnetic flux in the incoming CT, controlled by the CT formation in the CTA and subsequent loading by injection of gas and/or pellets, and (4) the radial distribution or gradient of impurity concentration, controlled by CT formation in the CTA and by impurity gas injection into the CT edges. Numerous previous papers[2,3,4] have shown that when a dense hot plasma has $p \gg B^2/2\mu_0$ within its volume (so called $\langle \beta \rangle \gg 1$, corresponding to $U_k/U_m \gg 1$), that impurity radiation near the plasma boundary leads to local edge temperature collapse, causing the hot plasma interior to expand, compressing the colder radiating boundary layer to higher densities and still higher edge radiation rates. This accelerating edge radiation proceeds until the temperature drops to such a point that the radiation stops due to plasma recombination or due to local optical depths approaching unity at the cavity black body temperature. The resultant steep temperature gradient between the hot plasma and the cold layer conducts heat into the cold layer, causing convection of hot interior plasma and magnetic flux into the cold layer which grows in thickness, <u>accreting</u> the particles
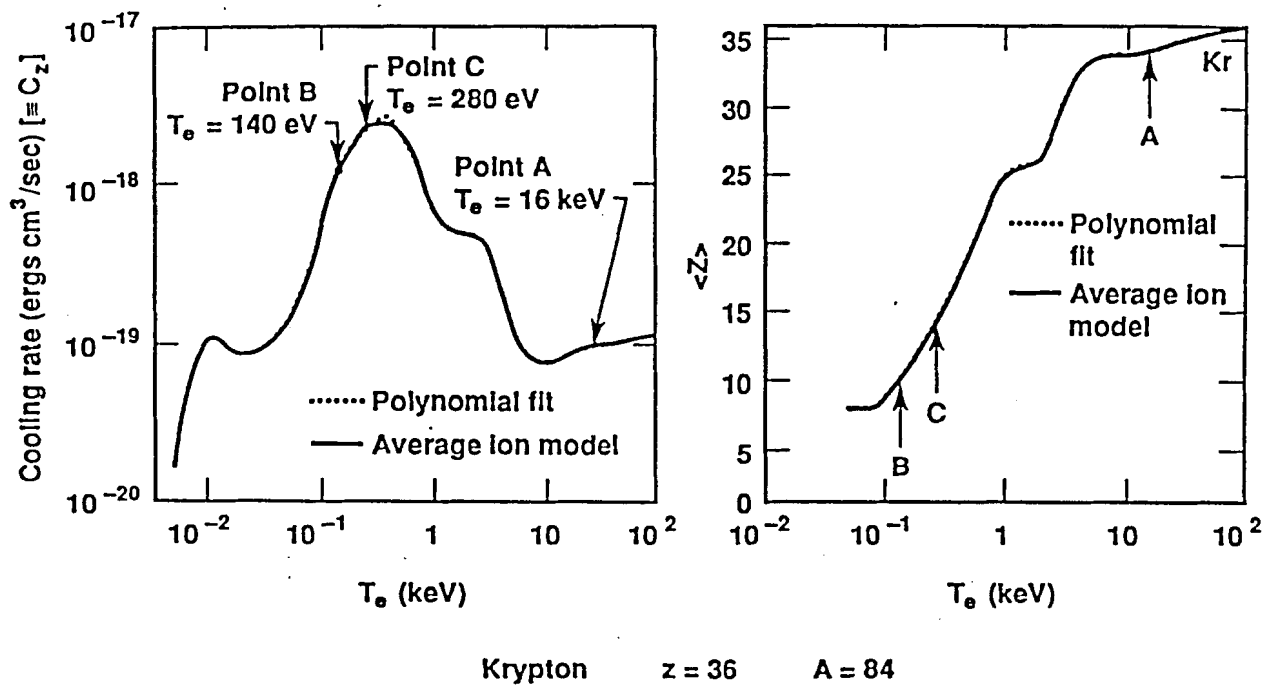
Fig. 2.2–1. Krypton impurity radiation rates per ion per electron as a function of T_e (optically thin). (From Post, Lokke, et al., PPPL–1352, July 1977.)

29

and flux. This process can be termed a "condensation wave" driven by nonuniform radiation losses under optically thin conditions. Rayleigh–Taylor and other mixing processes associated with the mass flow in these condensation waves need to be considered in future work.

Since the CT radiation decay time in this example (60 nsec) is long compared to hot plasma radial Alfvèn times (~1 nsec), radial pressure balance can be assumed over the whole CT volume:

$$p(r) + \frac{B^2(r)}{2\mu_0} = \frac{B_{wall}^2}{2\mu_0} \tag{2.2-1}$$

If we assume flux–plasma mass conservation over the plasma radial scale length,

$$\frac{n}{B} = \frac{n_e}{B_e}\left(1 - \frac{\psi}{\psi_w}\right)^{\alpha_n} = \frac{n_{fc}}{B_{fc}}\left(1 - \frac{\psi}{\psi_w}\right)^{\alpha_n} \tag{2.2-2}$$

$$\uparrow \qquad\qquad \uparrow$$

Entrance   Flux conserver

where $\alpha_n \gg 1$ is a profile index to vary in the CT preparation. Using Eq. (2.2-2), we can rewrite the pressure balance condition as

$$\frac{B^2}{2\mu_0} = \frac{B_w^2}{2\mu_0} - 2\,nT$$

$$= \frac{B_w^2}{2\mu_0} - \frac{2\,n_0\,T_0}{B_0}\left(\frac{T}{T_0}\right)\left(1 - \frac{\psi}{\psi_w}\right)^{\alpha_n} B \tag{2.2-3}$$

Equation (2.1-3) is quadratic in B

$$B = \frac{-b + \sqrt{b^2 - 4ac}}{2a} \tag{2.2-4}$$

with

$$a = \frac{1}{2\mu_0} \tag{2.2-5}$$

$$b = \frac{2 n_0 T_0}{B_0} \left(1 - \frac{\psi}{\psi_w}\right)^{\alpha_n} = \frac{\frac{2}{3} UK}{V_{CT} B_0} \left(1 - \frac{\psi}{\psi_w}\right)^{\alpha_n} \tag{2.2-6}$$

$$c = -\frac{B_w^2}{2\mu_0} \tag{2.2-7}$$

Most of the soft x–ray plasma bulk radiation from the condensation layer comes from the densest, coldest point of maximum thermal conductivity, where

$$\omega_e \tau_e = 1 = \frac{qB}{m_e} \frac{3.44 \times 10^5 \, T_{eV}^{3/2}}{10^{-6} \, n_H \left(1 + Z^2 f_z\right) \ln \Lambda_{ee}} \tag{2.2-8}$$

or where

$$T = 4.43 \times 10^{-2} \left[\frac{1 + Z^2 f_z}{2 + (1 + Z) f_z}\right]^{0.4} \left(\frac{P}{B}\right)^{0.4} \tag{2.2-9}$$

where T is in eV, $f_z \equiv n_{impurity}/n_{hydrogen}$, Z is the impurity ion charge (ave.) at temperature T, P is the plasma pressure in pascals, and B is in tesla. The characteristic width of the radiating $\omega_e \tau_e = 1$ layer is

$$\Delta x_e \approx 1.6 \times 10^{-19} \hat{k}_e \, T/Q \, (\text{meters}) \ , \tag{2.2-10}$$

where the radiation flux Q watts per square meter is given by

$$Q = \Delta x_e \, n_e \, n_z \, C_z \left(\frac{\text{watts}}{\text{m}^2}\right) \ , \tag{2.2-11}$$

31

where C_z is a function of T_e shown in Fig. 2.2–1 and the peak electron heat conductivity $\hat{k}_e$ (at $\omega_e \tau_e = 1$) is given by

$$\hat{k}_e = 3.55 \times 10^{22} \frac{T^{5/2}}{Z_{eff}} \, m^{-1} \, sec^{-1} \tag{2.2–12}$$

where

$$Z_{eff} = \frac{1 + Z^2 f_z}{1 + Z f_z} \, , \quad T \text{ in eV} \, . \tag{2.2–13}$$

Now, we can write

$$n_e \, n_z \, C_z = 3.91 \times 10^{37} \frac{f_z \left(1 + Z f_2\right)}{\left[2 + (Z) f_2\right]^2} C_z \frac{p^2}{T^2} \left(\frac{W}{m^3}\right) , \tag{2.2–14}$$

and then solving Eqs. (2.2–10) and (2.2–14) for Δx_e gives

$$\Delta x_e = 2.285 \times 10^{-21} \frac{\left(1 + Z^2 f_z\right)^{0.6}}{\left[2 + \left(1 + Z\right) f_z\right]^{0.1}} \frac{p^{0.1}}{B^{1.1}} \left(\frac{1}{\left(f_z C_z\right)^{1/2}}\right) \tag{2.1–15}$$

$$Q = 4.55 \times 10^{19} \frac{\left(f_z C_z\right)^{1/2} \left(1 + Z f_z\right) p^{1.3}}{\left[2 + f_z\right]^{1.3} \left(1 + Z^2 f_z\right)^{0.2} B^{0.3}} \tag{2.1–16}$$

The B used in the formulas Eqs. (2.2–15) and (2.2–16) is the flux density (B_x) compressed within the cold layer, which is related to the initial flux density B_0 just before the condensation wave front according to

$$B_x = B_0 \left[\frac{U_p \Delta x_e}{(\eta/\mu)} + 1\right] \qquad \text{tesla}$$

with

$$U_p = \frac{Q}{3/2 \, p} \qquad \text{m/sec}$$

$$\eta = 1.65 \times 10^{-9} \frac{Z_{eff} \, \ell n \Lambda}{\left(10^{-2} \, T\right)^{3/2}} \qquad \Omega\text{–m}$$

or

$$B_x \cong B_0 \left\{ 1 + 3.89 \times 10^{-6} \frac{(1 + Z\,f_z)\,p\left(1 + Z^2\,f_z\right)}{\left[2 + (1 + z)\,f_z\right]^2 B_x^2} \right\}$$

This gives a flux enhancement in the cold layer much smaller than the density increase in the cold layer due to magnetic diffusion $\delta_m \gg \Delta x_e$ ($a_{CT} \gg \delta_m$ skin depth $\gg \Delta x_e$).

Typically, with $p \sim 3 \times 10^{12}$ pa (30 Mbar), $f_z = 0.01$, $B = 10^3$ T (10 MG), $T \cong$ 300 eV, $Q \approx 10^{18}$ watts/m^2, and $\Delta x_e \cong 1$ micron.

The results of this model is applied to a specific set of initial profiles described in Fig. 2–3, and the resultant profiles at later times in the pulse are shown in Figs. 2.2–2 and 2.2–3. The total radiated power versus time is shown in Fig. 2.2–4. For comparison, a case with uniform profiles and impurity concentrations is shown also in Fig. 2.2–4. One sees that the effect of convection and compression in the condensation wave (due to high $\langle \beta \rangle$ and $U_k/U_m \gg 1$) result in a pulse shape much closer to the model calculation described in the previous section. Further stability studies by LASNEX are planned, which also will check the opacity (optical depth) and wall black body temperature. The optical depth of the cold layer is marginally thin to the radiation from the cold layer at temperature $T_{\Delta x_e} \cong 280$ eV. Should the approximation using optically–thin radiation rates turn out to be inappropriate at the parameters in Section 2.2, adjustments can be made in the initial impurity concentration (f_z) profile to result in cold layer radiation to occur at higher $T_{\Delta x_e} \geq 400$ eV, incurring a small penalty (~10%) in lower extraction efficiency.

Also, since the CT produces both hot plasma photons with $h\upsilon \geq T_{ehot}$ ~10 keV as well as soft x–rays from condensation layers with $h\upsilon \geq 4$–5 T_{ecold} ~1 keV, LASNEX calculations would also be needed to get the proper conversion of
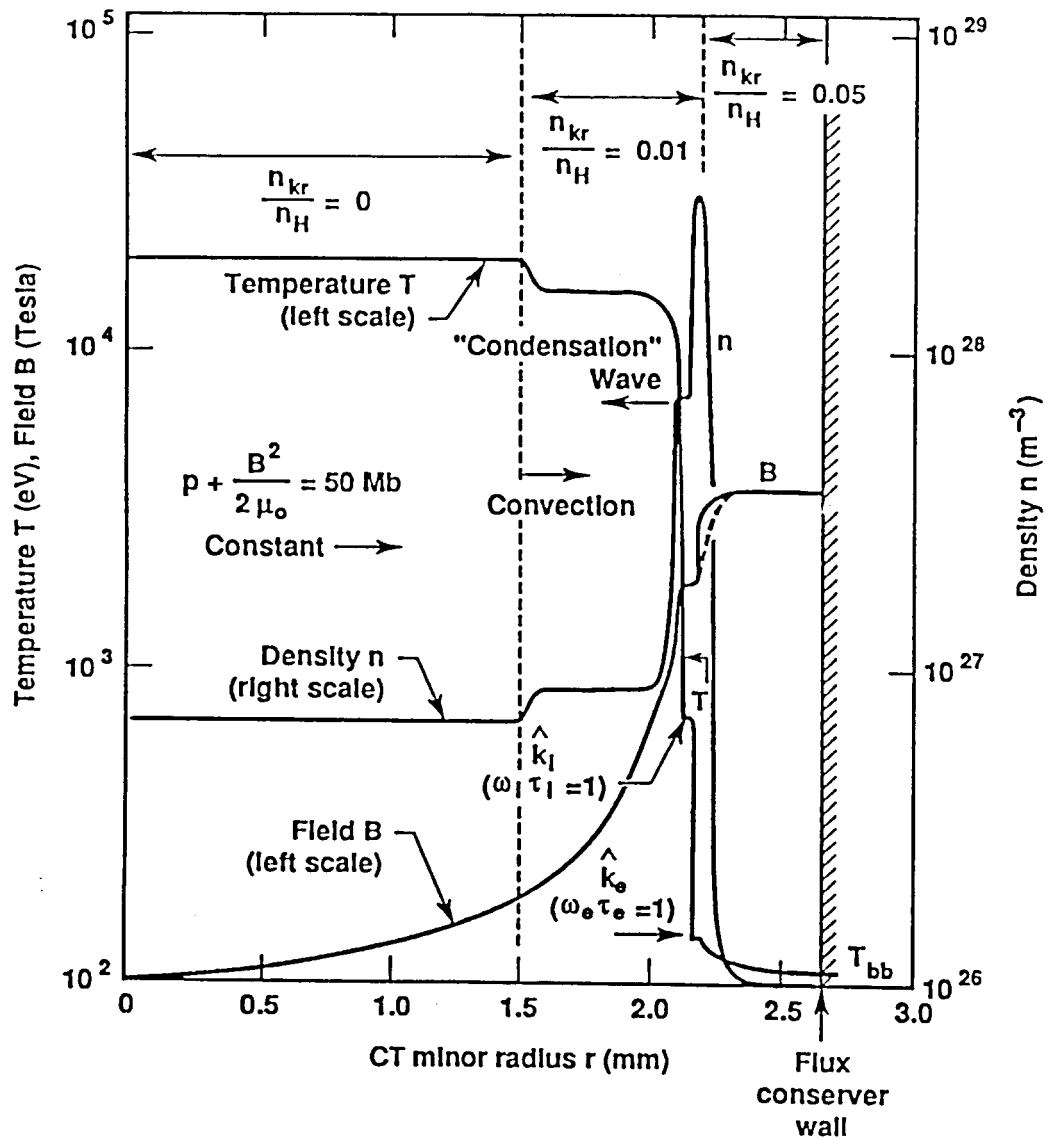
Fig. 2.2–2. Profiles of temperature T, density n, and field B for nonuniform impurity concentration n_{kr}/n_H, at time t = 53 ns (Point B), after beginning of radiation cooling front "condensation wave."
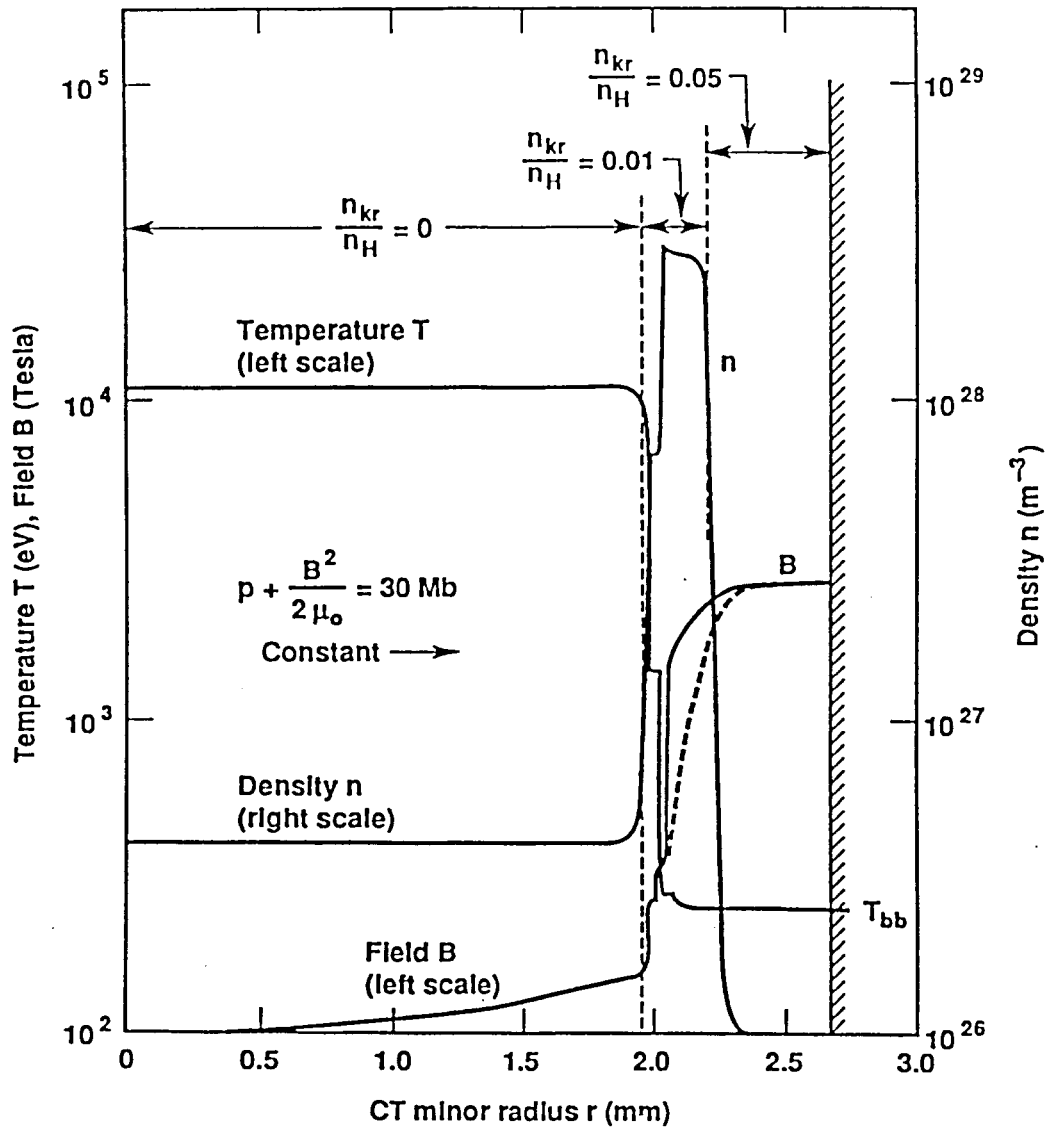
Fig. 2.2–3. Profiles of temperature T, density n, and field B for nonuniform impurity concentration n_{kr}/n_H, at time t = 57 ns (Point C), near peak of radiation output of the condensation wave.
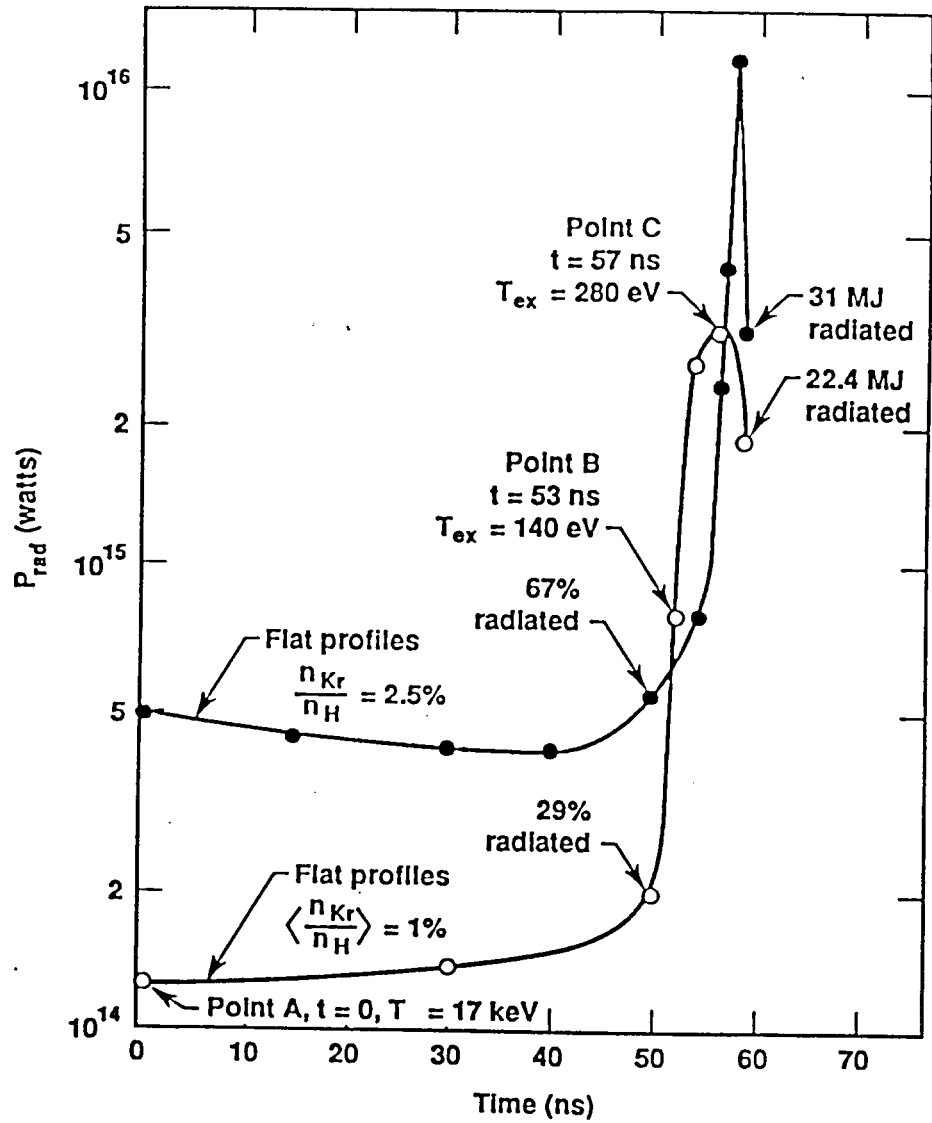
Fig. 2.2–4. CT radiated power versus time. Opacity–thin free–free, free–bound, bound–bound, $P_0 = 60$ Mbar, $E_0 = 40$ MJ, $T_0 = 20$ keV, $n_{Ho} = 8 \times 10^{26}$ m^{-3}, Krypton Seed.

the CT optically–thin radiation in the Marshak wall layer into reradiated blackbody radiation. Note the holes in the CT flux conserver (Fig. 2.2–1) are oriented to reduce capsule exposure to direct–line–of–sight 10 keV x–rays from the hot CT regions. Scaled down target experiments at relevant β and U_k/U_m are planned in the RACE facility in FY91–92.

References

1. S. G. Alikhanov, et al., *Nuclear Fusion* **10** (1973).

2. R. A. Gross, *Nuclear Fusion* **13**, 293 (1973).

3. R. E. Waltz, *Nuclear Fusion* **18**, 901 (1978).

4. J. Eddelman, private communications 1991. The RAC code is the Ring Accelerator Code. The TRAC code is the 2–D RAC code.

3.0 CT Accelerator and Transport System and Experimental Development Program Plan

The Compact Torus Accelerator (CTA) can serve as an efficient, low–cost–per–joule driver for ICF targets (Hartman, et al., 1987). Magnetically confined plasma rings are accelerated in a coaxial rail gun then focused to centimeter dimensions to provide a high–power, high–energy–density source for indirect drive of an ICF capsule. Relatively slow precompression and acceleration (tens of microseconds) allows the use of low–voltage capacitor banks, or possibly inductive storage, as the main driver source while high ring speed and focusing results in short energy delivery times (several nanoseconds). When combined with the high efficiency of rail–gun–like acceleration (about 50%), it appears feasible to consider CTAs of 100 MJ or higher that deliver 10s of MJ to a target for less than 10 $/J.

At LLNL we have constructed and are testing a proof–of–principle experiment, RACE (Ring ACcelerator Experiment), aimed at demonstrating acceleration of magnetically confined compact torus plasma rings to directed kinetic energies well in excess of their magnetic and thermal energies. The RACE apparatus (Fig. 3–1) consists of a magnetized coaxial plasma gun for compact torus ring formation (50 cm long, 35 cm outside diameter, 20 cm inside diameter) and coaxial acceleration electrodes. The gun has both inner and outer solenoids that can be energized to pre–establish a magnetic field. Gas is fed to the gun through eight electromagnetically driven valves that have a total plenum volume of 0.5 cm^3. The gas (H_2) is broken down and ejected from the gun by discharging a 60 kV, 200 kJ low–inductance capacitor bank between the inner and outer gun electrodes. As in similar magnetized gun experiments, firing the gun results in the emergence of a spheromak type of compact torus near the gun muzzle.

Vacuum vessel

Accelerator outer electrode

Accelerator center electrode

Compact torus plasma

Gun center electrode

Gun outer electrode

8 pulse gas valves

Outer solenoid

Inner
solenoid

To
accelerator
capacitor
bank

| 36 µF |
| 120 kV |
| 250 kJ |

Capacitor
bank

| 111 µF |
| 60 kV |
| 200 kJ |

To solenoid
capacitor
bank

| 0.03 F 5 kV 375 kJ |

Focusing
cone

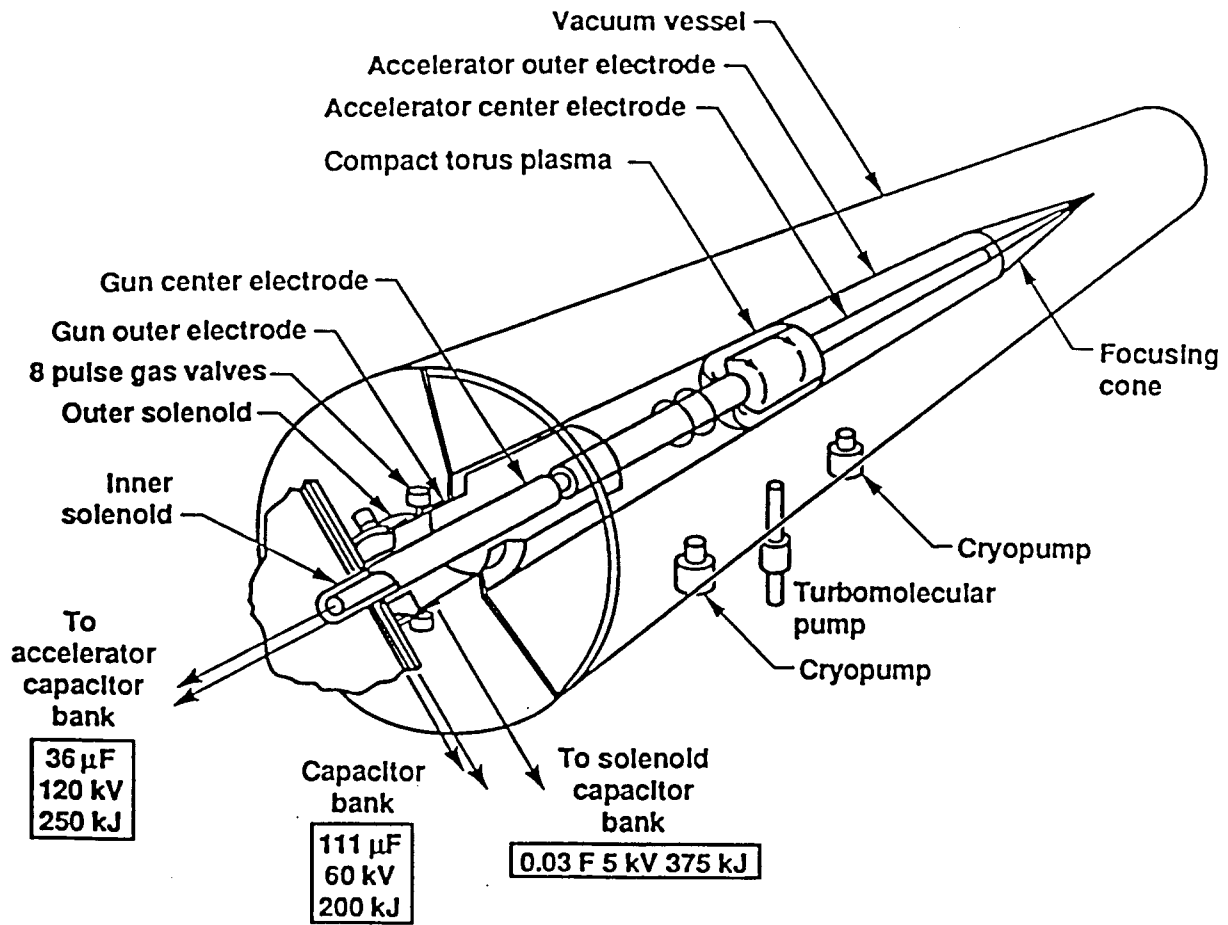Cryopump

Turbomolecular
pump

Cryopump

Fig. 3–1. Schematic of RACE.

In RACE, the ring is formed in the inter–electrode region at the beginning of the accelerator section. The coaxial accelerator electrodes are 4 m long (50 cm outside diameter, 20 cm inside diameter) with a 2–m long focusing cone. They are housed in a 1.5–m–diameter vacuum vessel. The accelerator is essentially a coaxial rail run with the ring acting as a moving short, accelerated by $J \times B$ forces when the 260–kJ, 120–kV capacitor bank is discharged. The center electrode of the accelerator passes through the center electrode of the gun and extends the length of the accelerator. The accelerating B field is fed through the annular slot between the inner gun and inner accelerator electrodes, as shown in Fig. 3–1.

Experiments conducted to date have verified the accelerator dynamics based on an axisymmetric magnetohydrodynamic model of ring acceleration (Hammer et al. 1988). In addition, acceleration forces exceeding predicted limits for Rayleigh–Taylor instability have been applied without significant disruption of the ring. Successful acceleration of low–mass rings (10 to 100 µg) up to 50 kJ kinetic energy and speeds of 1 to 2×10^8 cm/s (about 20 keV kinetic energy per nucleon) has been achieved at 30 to 40% efficiency. Initial experiments of ring focusing have exhibited the predicted field intensification as well as stagnation and bouncing of rings injected into the focus cone.

Experiments testing the slow pre–compression concept have successfully demonstrated a factor of 2 radial compression with the compressed CT fields, density and subsequent dynamics in the acceleration stage in good agreement with 2–D MHD calculations (Molvik, et al. 1990) (Hammer et al. 1991). The power density deliverable with the compressed CT's is $\simeq 2 \times 10^8$ W/cm^2. Experiments with an additional 740 cm long acceleration/focusing section are slated for the summer of 1991, and are predicted to yield another factor of 3 in radial compression (to 2.67 cm radius) with output power densities exceeding 10^{11} W/cm^2. A possible development path for the CTA technology is outlined in

Fig. 3-2, beginning with an upgrade of the existing RACE device to ≃ 1 MJ accelerator bank energy.

Scaling of the CTA to a high energy appropriate for ICF driver applications has been considered using a point design based on the verified model of acceleration using the RAC (Ring Acceleration Code) O-D Code. Reasonable constraints on the maximum B-field (less than 300 kG) and wall heating by ring radiation have been applied; however, detailed considerations in this area await experimental study. A point design model for a 100-MJ (driver bank energy) CTA, ICF driver is summarized in Table 3-1. This CTA design, which uses a precompression cone, is 30 m long and delivers 36 MJ of focused ring energy at a 1.1-cm ring radius. For reactor evaluations, a target gain of 50 is used, assuming that an indirect drive capsule can be designed to convert the ring kinetic energy into properly pulse-shaped radiation. At a rate of 1.5 pulses per second (pps), this driver would correspond to a 500 MW$_e$ fusion power plant.

The primary cost of a CTA driver is the energy storage system for the accelerator. (In Table 3-1 a capacitive energy storage is assumed.) Because the acceleration time is relatively long (8 μs to peak current), the bank can be low voltage and have relatively high inductance (2.5 μH). Consequently the energy storage cost can be low (0.06 $/J capacitor cost for a 5×10^4 shot lifetime), as shown in Table 3-2 for an off-the-shelf, 100-MJ, 500-kV capacitor bank. Here the total driver bank cost for a 5×10^4 shot lifetime is estimated to be 0.35 $/J ($35M/100 MJ). To increase the lifetime to 3×10^7 shots or a 1 year lifetime, the capacitors must be operated at a factor $(3 \times 10^7 / 5 \times 10^4)^{1/7}$ or 2.5 lower voltage than their rated value. This increases the cost/Joule from 0.06 $/J to 0.06 $(2.5)^2$ $/J or 0.38 $/J for capacitors, raising the total bank cost to 0.67 $/J. The capacitor replacement cost is an acceptably low fraction (0.14) of the annual electrical revenue.

$10^{11} W/cm^2$ $10^{13} W/cm^2$ $10^{15} W/cm^2$ $10^{16} W/cm^2$

FY   91   92   93   94   95   96   97   98   99

RACE + 1 MJ upgrade
($5M/year)

10-20 MJ bank energy
($10M/year)

100 MJ bank energy
(~$30M/year)
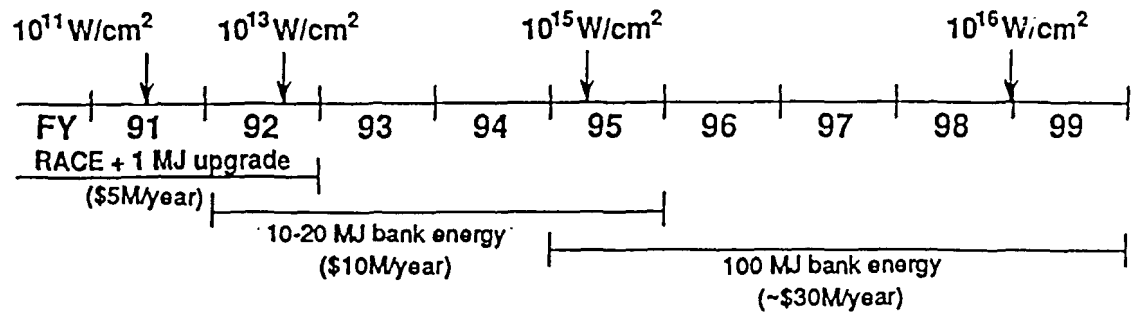
02-15-0490-1986

Fig. 3-2. An upgrade of RACE to 1 MJ, followed by higher energy experiments would demonstrate relevance to ICF.

Table 3–1. 100–MJ compact torus accelerator for ICF.[a]

Accelerator bank energy	100 MJ
Accelerator bank voltage	2.5 MV
Accelerator length	30 m
Initial ring radius	100 cm
Initial ring magnetic energy	50 kJ
Ring mass	2 mgm
Peak accelerator current (t = 8 ms)	5.6 MA
Ring B–field during acceleration	280 kG
Focused ring radius	1.1 cm
Focused ring length	0.5 cm
Focused ring kinetic energy	36 MJ
Focused ring velocity	600 cm/ms
Focused ring magnetic energy	3 MJ
Focused ring magnetic field	20 MG
Target gain	50
Fusion yield	1800 MJ
Pulse rate	0.8 pps
Bank life (1 yr)	3×10^7 shots
Shot life revenue (50 mill COE)	$265M
Bank cost	$50M
Capacitor cost	$35M
Capacitor cost/1 yr revenue	0.14

[a]Point design using RAC code

Table 3–2. Cost accounting of a 100 MJ, 500 kV CTA capacitor bank.[a]

System	Cost ($K)
Marx module	11,826
Inductor module	768.4
Cables trans. line	330
Water trans. line	1,010
Coupler	439
Trigger system	1,195
Charging system	1,696
Crowbar system	20
Module frame structure (includes assembly)	2,300
Capacitor testing (500 shot cap.; 10 at a time)	728.3
Bank performance monitoring system	909
Oil system (includes assembly)	795
Complete system testing	784
Miscellaneous	475
Preliminary cost	23,276
Contingency costs (factor, amount)	3,491
Preliminary total cost	26,767
Design (preliminary total cost factor, amount)	4,015
Management/coordination (P.T.C. factor, amount)	1,338
Total cost	32,121
Fee (8% of total cost)	2,570
Adjusted total cost	34,691

[a]Concept and Cost Estimates by Pulse Sciences, Inc., PSI–FR–365, April 1988.

Clearly the energy and power density achieved near the ring focus greatly exceeds material limits (Table 3–1). Final focusing and transport of the ring to the target inside the reactor containment vessel can be provided by a disposable end section of the CTA, as shown in Figs. 1–3 and 1–4. Because the ring residence time at any point along the end section is short (a few nanoseconds), the mass of the disposable end section can be small (8 kg or less) and the section can be replaced for each shot at an acceptably low cost.

Appropriate targets for the RACE driver are discussed in section 2. The design must shape the pulse appropriate to an indirect drive target (see section 2).

References

1. Hartman, C. W., J. L. Eddleman, J. H. Hammer, and D. L. Meeker (1987), "The Compact Torus Plasma Ring Accelerator—A New Type Driver for Inertial Confinement Fusion," in *Proc 4th Internat. Conf. on Energy Nuclear Energy Systems, June 30–July 4, 1986, Madrid*, G. Velarde and E. Minguez, Eds. (World Scientific Publishing Co., Singapore).

2. Hammer, J. H., C. W. Hartman, J. L. Eddleman, and H. S. McLean (1988), "Experimental Demonstration of Acceleration and Focusing of Magnetically Confined Plasma Rings," *Phys Rev Lett*, 61, 2483.

3. Molvik, A. W., et al., *Phys Rev Lett*, 66, 165 (1991).

4. Hammer, J. H., et al., to be published in *Phys Fluids B*, 1991.

4.0 Target Description, Production, and Injection

Introduction and Conclusions:

The target assembly, including the compact torus guide cone, are described in this section. A possible method of producing the target assemblies is given. The preferred method for injecting the target assemblies requires the launching holde to travel to the top of the reactor chamber clearing any Flibe out of the target assemblies path. To reduce stresses in the target assembly during launching to a reasonable level we recommend the repetition rate be reduced from 1.5 Hz to 1 F or slightly lower. We have not yet determined a suitable support method for the inner cone.
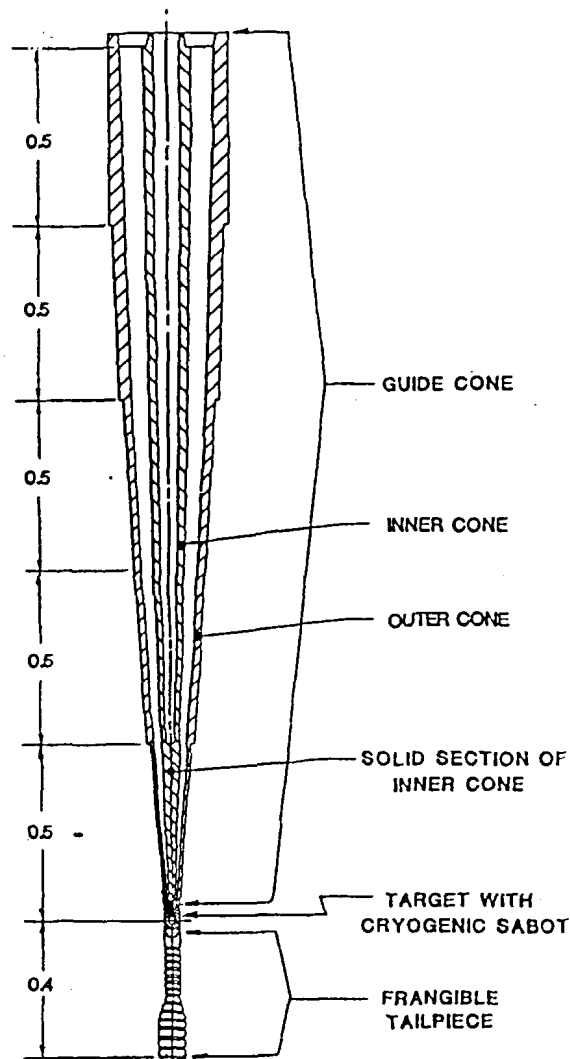
Fig. 4-1. Target assembly.

4.1 Target Description and Production

The target assembly that will be injected into the reactor chamber consists of three sections as shown in Fig. 4–1. They are the guide cone, the target with cryogenic sabot, and the frangible tail piece.

The guide cone directs the compact torus from the end of the accelerator at the upper reactor chamber wall to the target. It is made out of frozen room temperature Flibe and consists of an outer cone and an inner cone, each about 2 mm thick. The bottom 60 cm of the inner cone is solid. The guide cone may be at room temperature.

The target with its hohlraum are maintained at cryogenic temperatures (4 K) by being surrounded by a sabot of cryogenic Flibe.

A room temperature frangible (shatterable) tailpiece is added to protect the lower reactor closure and entrance system from neutron damage.

A direct drive ICF Target Factory Model is being developed.[1] The process used to manufacture capsules may be applicable to indirect drive targets including the compact torus. The capsule production technique is represented in Fig. 4.1–1.

Using the microencapsulation technique, shells of polystyrene are formed by injecting a liquid layer of polystyrene, and sandwiched between two aqueous layers, into a water bath through cylindrical, triply concentric nozzles. These spherical shells are swept out of the column and the solvent and water removed. It has been shown that very smooth, spherical shells can be mass produced by this technique although reactor-sized shells have not been demonstrated. We assume that this process can be scaled to the required production rates, sizes, and quality by implementing the above scheme. The fabricated capsules would undergo inspection and be placed in canisters in order to be filled with DT fuel and cooled down.
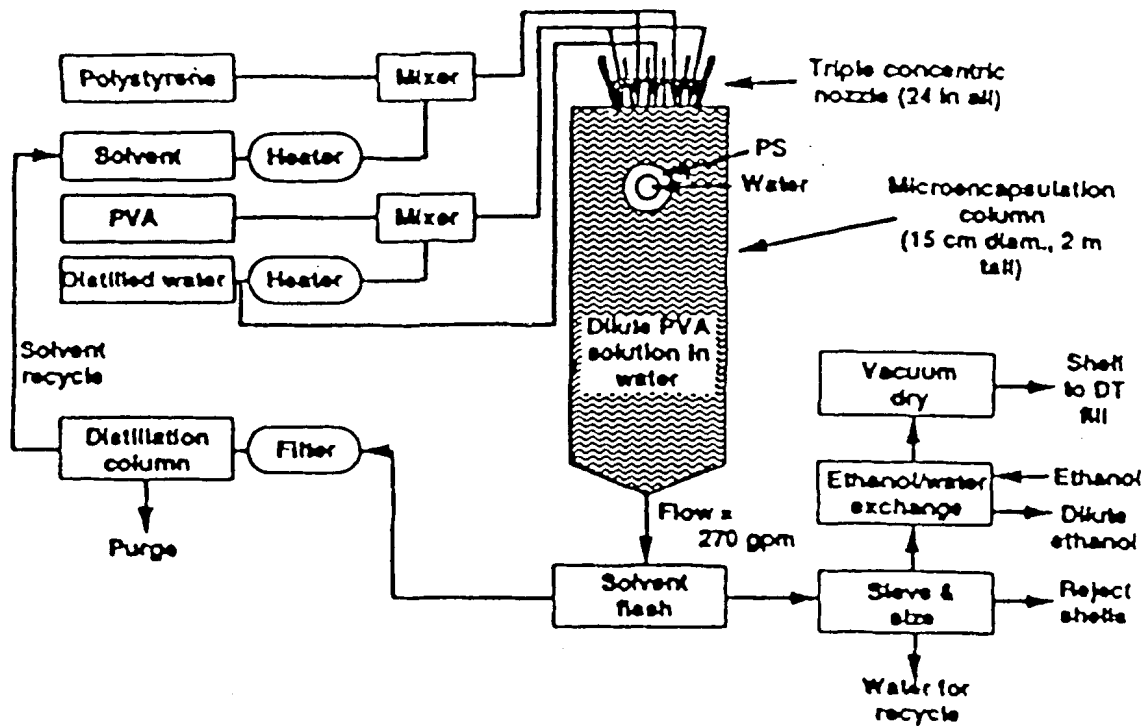
Fig. 4.1–1. Schematic of assumed capsule fabrication.

The most viable fill method is to diffuse DT gas into the capsule through the polystyrene (containing carbon and hydrogen) shell. Quicker methods-such as drill and plug-result in intolerable roughness to the capsule's surface. We estimate that about 40 h is required to fill the capsule. Fill in time depends on the ratio of the surface area to mass of diffused DT as well as the shell thickness. Higher yield capsules take slightly longer to fill. Thus, a DT inventory corresponding to the DT fuel required for about forty hours of reactor operation is dictated by this step in the process.

After filling, the capsules are cooled down to just below the triple point of DT-about 18 K-so that the capsules are depressurized. The DT plates uniformly onto the inside of the polystyrene capsule via the process known as β-layering. This latter process is assumed to require about 30 minutes. The β-layering process has yet to be demonstrated for low-conductivity capsules.

The estimated tritium inventory for the target factory is about 4 kg, about half of this tritium is in the capsule fill canisters and half in the associated piping.

The capsules would be placed inside the hohlraum much as in heavy ion targets. The cryogenic hohlraum held at 4 K would then be encased in a cryogenic sabot. The assembly could then proceed as in Fig. 4.1–2.

The sabot could be attached to the tailpiece and placed in a retrievable launching holder. The guide cone could then be positioned above the sabot in the launching holder. The outer cone could be well supported by the holder resting on machined surfaces as shown. We have not yet determined a suitable support method for the inner cone.

Assuming the inner and outer guide cones are 2 mm thick, the masses and temperatures of the target assembly parts are given in Table 4.1–1.

The cost for materials for these target assemblies should be about the same as for more conventional targets since the Flibe is reusable. If we assume a target cost of 7 mills per kWh is acceptable and assume a 1800 MJ yield with an electrical

power to fusion power ratio of 0.38, then $1.34 per target would be an acceptable target cost. This acceptable cost scales linearly with yield and with conversion efficiency.

Then $t_1 = 0.32$ s

$\upsilon_1 = 19.2$ m/s

$\upsilon_2 = 15.7$ m/s

$z_1 = 3.1$ m

FLBE ICICLE ENTERING
LAUNCHING HOLDER

RETRIEVABLE
LOW-MASS
LAUNCHING HOLDER

ASSEMBLED UNIT
READY FOR LAUNCHING
OR
CRYOGENIC STORAGE
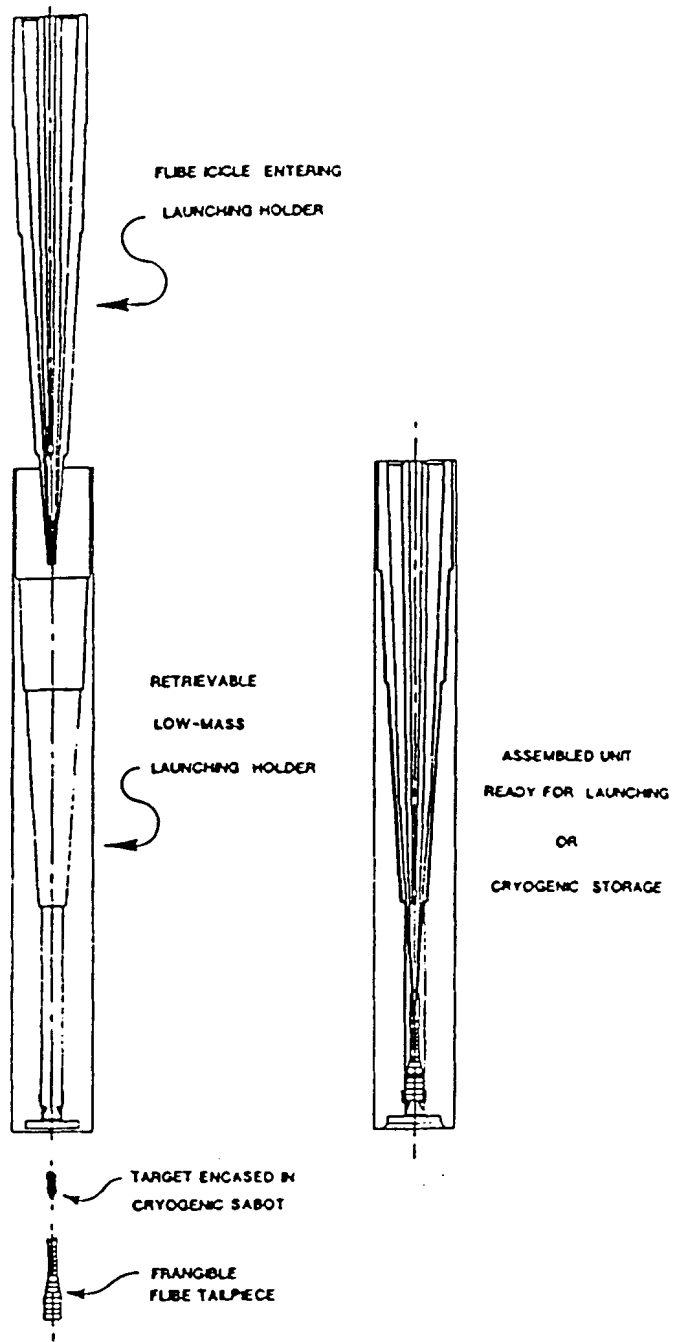
TARGET ENCASED IN
CRYOGENIC SABOT

FRANGIBLE
FLBE TAILPIECE

Fig. 4.1–2. Assembling the target assembly.

Table 4.1-1. Masses and Temperatures of Target Assembly Parts

Item	Temperature (K)	Mass (g)
Target and Sabot	4	400
Inner cone	300	2600
Outer cone	300	3100
Frangible Tail Piece	300	2300

4.2   Target Assembly Injection

Once the target assemblies are assembled in the launching holders they can be moved to the launching ram as shown in Fig. 4.2–1.

The base of the launching holder is clamped to the top of the charging ram. The ram then accelerates upward, pushing the launching holder and target assembly part of the way to the top of the chamber. The charging ram and holder are then accelerated downward, allowing the target assembly to coast under the influence of gravity to the top of the chamber. Just as the target assembly reaches the top of the reactor chamber, the compact torus passes through the guide cone. The pressure exerted by the compact torus will shatter the guide cone as the compact torus passes through. The compact torus then produces the micro explosion. The launching holder must be withdrawn from the chamber prior to the fusion micro explosion. The ram must be returned to its original position, the holder removed and a new holder with target assembly placed on the ram before the cycle can be repeated.

The reactor has an assumed repetition rate (F) of 1.5 Hz. This leaves 2/3 sec for the target assembly to be injected a distance (d) to the top of the reactor chamber. This injection is accomplished by accelerating the target assembly upward with an assumed constant acceleration (a_1) for a time (t_1) reached a velocity of v_1. The holder is then retracted and the target assembly coasts under gravitational acceleration to the top of the reactor chamber at a time $t_2 = 2/3$ sec.

Let z be the height of the target assembly above its pre-injection position. Then for $t_1 \leq t \leq t_2$, $z = 1/2 a_1 t_1^2 + (a_1 t_1)(t - t_1) - 1/2 g (t - t_1)^2$. For $z = d$, $t = t_2 = 2/3$ sec. We assume d = 9 m, $a_1 = 200$ m/s^2 and solve for the unknown t_1. $t_1 = 0.086$ sec. Knowing t_1, we can solve for z_1, and v_2. $v_2 = 11.4$ m/s. $z_1 = 1.48$ m.
The target assembly may be fragile and the maximum acceleration (a_1) that it can sustain without damage may be less than 200 m/s^2 The inner guide cone may be
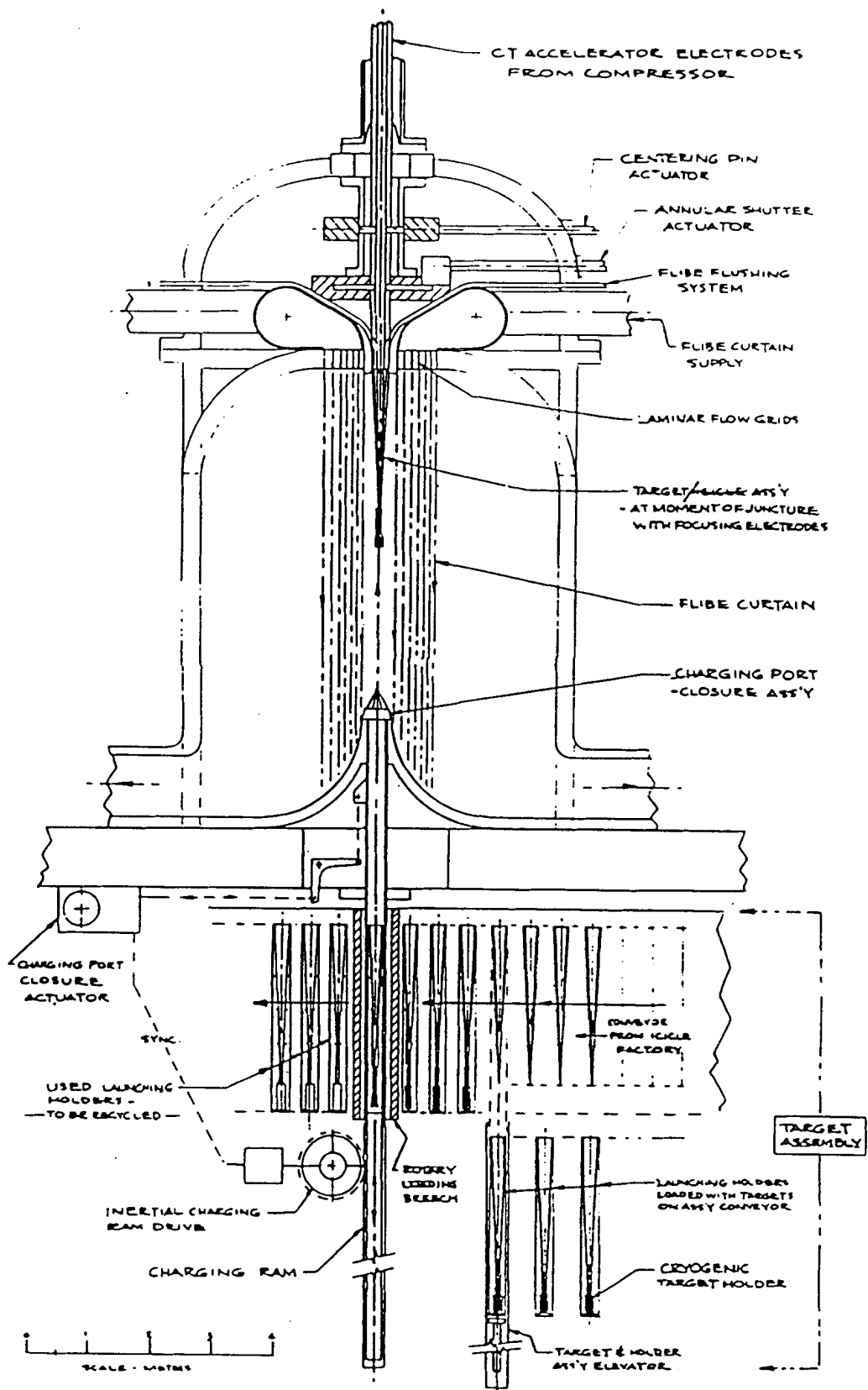
Fig. 4.2–1. Reactor chamber with launching mechanism.

This page intentionally left blank.

the target assembly may have Flibe droplets in it. The Flibe would enter the target assembly with one or more of the following adverse effects.

1. The Flibe droplets may break the target assembly walls.

2. The Flibe droplets may deflect the target assembly causing internal misalignment of the inner and outer cones or causing misalignment of the entire assembly as it reaches the top of the reactor chamber.

3. The Flibe droplets may partially fill the assembly channel through which the compact torus must pass.

To avoid the problem of the target assembly hitting Flibe, we must either ensure the path is clear of Flibe or design a launching holder that travels with the target assembly to the top of the chamber. A holder which is considerably longer than the target assembly could be injected all the way to the top of the reactor chamber clearing the path of Flibe. The holder could then be retracted and its cover opened while the target assembly continues to coast up to the chamber top. We assume the target holder to be 6 m longer than the target assembly. The one way distance traveled by the holder is 9 m. The target assembly injection distance is now 15 m.

To operate at 1.5 Hz, this system would require very rapid motion ($\sim$140 m/s) and large acceleration of the holder ($\sim$2100 m/s^2) and rather large target assembly acceleration ($\sim$180 m/s^2).

The accelerations and velocities just described for the 9 m long holder and target assembly may be too large. For example, the accelerations could be limited to 50 m/s^2 for target assembly and 500 m/s^2 for the holder. These could be accommodated with a cycle time of 1.14 s with a holder that is only 7 m long.

In this scenario, the total target travel distance is (9 + 4)m = 13 m. At cycle time t = 0 the target assembly and holder begin acceleration at 50 m/s^2 for 0.4 s reaching velocity 20 m/s and height 4 m. They move together at constant velocity to height (13 − 4.4)m = 8.6 m requiring an additional time of 0.23 s. At time 0.63 s

56

the target assembly begins coasting to chamber top for an additional 0.23 s and explodes at 0.86 s. At time 0.63 s the holder begins deceleration and is stopped at chamber top at 0.67 s. The holder then travels down and clears the chamber at time 0.83 s and is fully lowered at time 0.94 s. A new holder is in place on launcher at time 1.14 s and the cycle can repeat. To reduce the stress from acceleration we recommend a larger cycle time of about 1.14 s or 0.88 Hz repetition rate.

Further study is required to determine a suitable support method for the inner cone. Perhaps retractable "fingers" from the launching holder through slits in the outer cone could be used. If these "fingers" are vertical the cone could slide off them.

5.0 Balance of Plant for the Compact Torus ICF Reactor

A block diagram of the fusion power plant is shown in Fig. 5-1. The balance of plant (BOP) consists of the vacuum disengager and all the components to the right of it. Part of the primary Flibe coolant from the reactor goes to the Flibe vacuum disengager (FVD) and the rest of the flow is bypassed as shown on Fig. 5-1. The Flibe flow to the FVD is selected to result in the lowest COE (cost of electricity) contribution for the BOP while satisfying all the key temperature constraints (Hoffman, 1991).

The Flibe is sprayed into the top of the FVD as a fine mist so that most of the tritium can diffuse out of the Flibe in the fall time. The design goal is to remove about 99% of the tritium in the FVD before the Flibe enters the IHX's (intermediate heat exchangers) (Dolan and Longhurst, 1990). Each IHX is a shell and tube counterflow design with Flibe on the tube side and sodium fluoroborate ($NaBF_4$) on the secondary shell side. Typically, each of the three IHX's handles a nominal thermal power of about 1000 MWth and consists of about 7000 tubes of 2 cm outer diameter in a tube bundle about 11 meters long and 2.5 meters in diameter. The large heat transfer surface area of the IHX's allows about 6.5% of the remaining tritium to diffuse across to the $NaBF_4$ (Longhurst and Dolan, 1990).

The Flibe flows from one component to the next in double–walled piping with a helium purge flow in the annular space. The tentative material choice for the inner pipes is Hastelloy N, which is the same as that selected for the IHX's. All the helium purge gas flows to a helium purification system where the tritium is removed for use in the target factory. The molten salt pumps are scaled–up versions of the pump designs proposed for the Molten Salt Breeder Reactor (Rosenthal, et. al., 1972).

In order to reduce the tritium in the $NaBF_4$ flow before it reaches the steam generators, a tritium decontamination unit must be employed, as shown in Fig 5-1.
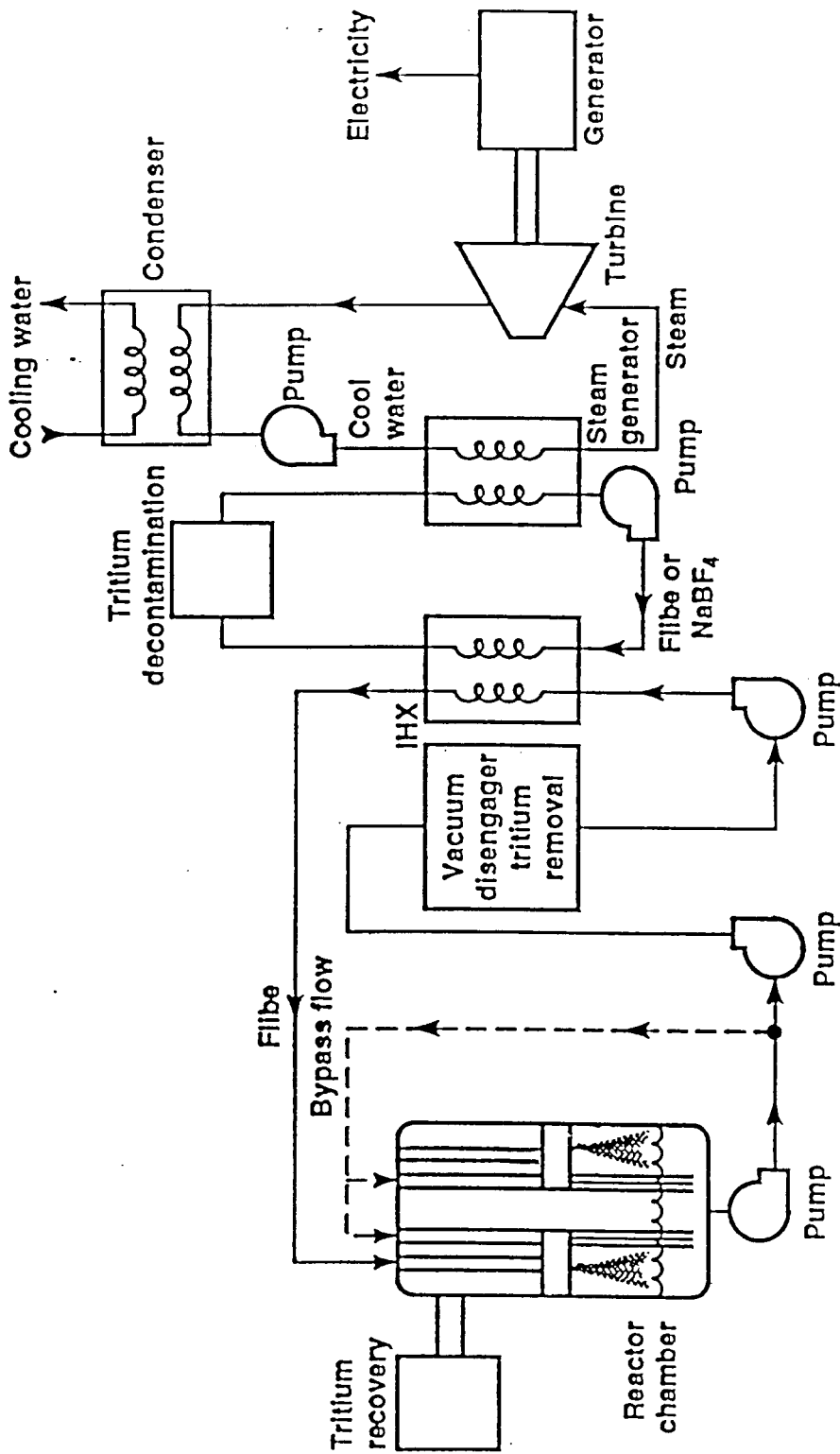
Fig. 5-1. Block diagram of the fusion power plant showing the key components of the BOP (balance of plant).

This unit consists of a gas evolution column (GEC) using helium gas in counterflow to the downward flowing $NaBF_4$ and a helium purification system. The design goal is to remove 99% of the tritium from the $NaBF_4$ before it flows into the steam generators. When these goals are met, less than 40 Ci/day of tritium will diffuse across the steam generator tubes into the steam flows (Dolan and Longhurst, 1990).

The steam generator design is based on the Clinch River Breeder Reactor (CRBR) steam generators (Moody and Gabler, 1978). Each steam generator has a nominal rating of 1000 MWth and consists of two evaporators and one superheater. The evaporators and superheaters have a counterflow, hockey stick geometry (very similar to the CRBR design). Each evaporator has an active tube length of about 10 meters and a tube bundle diameter of about 1.7 meters, and the steam/water flow exits at a quality of 0.50. The steam from two evaporators is separated from the water and flows into the superheater. Each superheater has an active tube length of about 17 meters and a tube bundle diameter of about 2.0 meters (Hoffman and Lee, 1991). The material for the evaporators and superheaters has tentatively been chosen as Hastelloy N, the same as for the IHX's.

The steam produced in the steam generators enters the high-pressure steam turbine of the steam power plant (SPP) at about 790 K and 16 MPa. The SPP employs a fully-regenerative, non-reheat cycle with six feedwater heaters. Assuming a condensation temperature of 320 K, the thermal efficiency of the SPP is calculated to be 41.5%. Preliminary estimates indicate that the BOP will contribute between 30 and 40 mills/kWh to the cost of electricity of the fusion power plant (Hoffman and Lee, 1991) in 1988 dollars.

References

T. J. Dolan and G. R. Longhurst (1990), "Safety and Environmental Aspects of HYLIFE-II," Fusion Technology 19, 1392 (1991).

M. A. Hoffman (1991), "The Heat Transport System and Plant Design for the HYLIFE-II Fusion Reactor," Fusion Technology 19, 625.

M. A. Hoffman and Y. Lee (1991), "Performance and Cost Analysis of the HYLIFE-II Balance of Plant" (in preparation).

G. R. Longhurst and T. J. Dolan (1990), "Tritium Permeation Losses in HYLIFE-II Heat Exchanger Tubes," Fusion Technology 19, 820.

E. Moody and M. J. Gabler (19780, "Heat Transfer with Hockey-Stick Steam Generators," General Electric Report GEFR-SP-070, Sunnyvale, CA, Revised March 1978.

M. W. Rosenthal, P. N. Haubenreich and R. B. Briggs (1972), "The Development Status of Molten-Salt Breeder Reactors," Oak Ridge National Laboratory Report ORNL-4812.

6.0 Economic Analysis

The main difference between the CT reactor design and HYLIFE-I is the use of a low cost driver. Both the CT reactor and HYLIFE-I have a yield of 1.8 GJ and a repetition rate of 1.5 Hz. HYLIFE-II is a low gain (~70) low yield (350 MJ) high rep rate (~8 Hz) version of the HYLIFE design using a "conventional" heavy ion driver having a direct cost of about $1.4B. The CT driver is expected to have a direct cost of $200M or less. Using the SAFIRE code we have calculated the cost of the components and cost of electricity (COE), which is 4.8 ¢/kWh for a $200M driver in 1988 dollars. The results are given in Tables 6–1 and 6–2.

The SAFIRE code (McCarville, et al., 1987) evolved from a code developed by TRW and LLNL in 1979 to evaluate the performance of fusion-fission hybrid reactors. The code was updated and modified to model ICF power plants, and was recently used to model HYLIFE-II based power plants (Bieri, 1991). The cost estimates in this paper were obtained by using the SAFIRE (Bieri, 1991) models for HYLIFE-II reactor chambers along fixed values for driver energy (40 MJ), target gain (45), and driver cost (either $200M or $1,000M). Target costs were included, but no attempt was made to include the costs associated with fabrication or placement of the final focusing assembly which must be replaced between shots. All costs were assumed to be in constant 1988 dollars and construction time was assumed to be 8 years.

To show the important effect of the low cost driver, we plot COE versus driver cost in Fig. 6–1. At $200M, direct cost, the driver adds 15% to the COE and 15% to the total direct cost, that is, it is not a dominant cost item. At $1.4B the driver would have added 100% to the COE.

In Section 5.0 the balance of plant was quoted as contributing 3 to 4 ¢/kWh. The items not included were driver design, target factory, tracking and alignment systems, first wall, and blanket and shield. From Table 6–2 we see these items added about 40% or about 1.2 ¢/kWh to the COE of the balance of plant alone.

Table 6-1. Overall plant performance summary.

DESCRIPTION:
    DRIVER TYPE: COMPACT TORUS
    GAIN CURVE: ONE-SIDED CT
    CHAMBER TYPE: HYLIFE-II
    NUMBER OF CHAMBERS PER UNIT: 1
    NUMBER OF UNITS PER PLANT: 1
    NUMBER OF DRIVERS: 1
    NUMBER OF TARGET FACTORIES: 1

PLANT PARAMETERS:
    CHAMBER PULSE RATE (HZ):   1.50
    DRIVER ENERGY (MJ):   40.00
    TARGET GAIN: 45.0
    TARGET YIELD (MJ):   1800.0
    THERMAL POWER (MWT):   3096.0
    THERMAL CYCLE EFFICIENCY (%):   38.6
    HEAT REJECTED (MWT):   1901.0
    AVAILABILITY FACTOR (%):   75.0

ELECTRIC POWER BALANCE (MWE):
    GROSS ELECTRIC POWER: 1195.1
    DRIVER POWER/UNIT: 157.9
    PUMPING POWER: 3.7
    OTHER BOP POWER: 0.0
    NET ELECTRIC POWER: 1033.4

DRIVER OUTPUT ENERGY=40.00 MJ
DRIVER EFFICIENCY=0.380
DRIVER INPUT ELECTRICAL ENERGY PER SHOT= 105.26 MJ
DRIVER REPETITION RATE= 1.50 SHOTS/SEC
REQUIRED INPUT ELECTRICAL POWER PER DRIVER= 157.89 MWE

ECONOMIC FACTORS (%):
    ESCALATION RATE: 6.00
    GENERAL INFLATION RATE: 6.00
    AFTER-TAX COST OF MONEY: 9.00
    REAL COST OF MONEY: 2.83
    CURRENT DOLLAR FIXED CHARGE RATE: 16.22
    CONSTANT DOLLAR FIXED CHARGE RATE: 8.32

Table 6–2. ICF economic evaluation for 1 unit power plant.

ACCOUNT	ACCOUNT TITLE	M$
20	LAND AND LAND RIGHTS	5.0
21	STRUCTURES AND IMPROVEMENTS	296.8
22	REACTOR PLANT EQUIPMENT	563.5
23	TURBINE PLANT EQUIPMENT	233.3
24	ELECTRIC PLANT EQUIPMENT	92.5
25	MISCELLANEOUS PLANT EQUIPMENT	60.2
26	MAIN HEAT REJECTION EQUIPMENT	39.9
27	DRIVER EQUIPMENT	220.9
28	TARGET FACTORY EQUIPMENT	85.4
	TOTAL DIRECT COST	1597.5
91	CONSTRUCTION SERVICES	319.5
92	HOME OFFICE ENGINEERING AND SERVICES	239.6
93	FIELD OFFICE ENGINEERING AND SERVICES	159.8
94	OWNER'S COST	111.8
95	PROJECT CONTINGENCY	242.8
	TOTAL OVERNIGHT COST	2671.1

		CURRENT$	CONSTANT$
96	ESCALATION DURING CONSTRUCTION	862.0	0.0
97	INTEREST DURING CONSTRUCTION	1121.9	249.5
	TOTAL CAPITAL COST	4655.0	2920.6

COST OF ELECTRICITY	CURRENT$	CONSTANT$
CAPITAL	11.12	3.58
FUEL	0.03	0.01
O&M	3.67	1.18
TOTAL	14.82	4.77

CONSTANT $ RESULTS IN 1988 DOLLARS
CURRENT $ RESULTS IN 1996 DOLLARS

22 REACTOR PLANT EQUIPMENT COSTS (M$) ....

	M$
TRACKING,ALIGN SYSTEMS	30.4
FIRST WALL SYSTEMS	4.1
T EXTRACTION SYSTEMS	27.3
BLANKET AND SHIELD	106.6
HEAT TRANSPORT SYSTEM	395.1*
22.00 TOTAL RPE COST	563.5

23 TURBINE PLANT EQUIPMENT COSTS (M$)....

		M$
23.01	TURBINE GENERATORS	132.9
23.02	NOT CURRENTLY USED	
23.03	CONDENSING SYSTEMS	36.9
23.04	FEED HEATING SYSTEMS	25.2
23.05	OTHER TP EQUIPMENT	24.4
23.06	INSTRUMT. AND CONTROL	6.4
23.07	MISCELLANEOUS ITEMS	7.5
23.00	TOTAL TPE COST	233.3

24 ELECTRIC PLANT EQUIPMENT COSTS (M$)....

		M$
24.01	SWITCHGEAR	13.3
24.02	STATION SERVICE EQUIP	20.1
24.03	SWITCHBOARDS	2.0
24.04	PROTECTIVE EQUIPMENT	3.5
24.05	ELECT STRUCTS + WIRNG	28.8
24.06	POWER + CONTRL WIRING	24.8
24.00	TOTAL EPE COST	92.5

25 MISCELLANEOUS PLANT EQUIPMENT COSTS (M$)....

		M$
25.01	TRANSP. + LIFT EQUIP	6.5
25.02	AIR,WATER AND STEAM	38.4
25.03	COMMUNICATIONS EQUIP	8.7
25.04	FURNISHINGS + FIXTURES	3.1
25.05	WASTE WATER TREATMENT	3.5
25.00	TOTAL MPE COSTS	60.2

26 MAIN HEAT REJECTION SYSTEM COSTS (M$)..

		M$
26.01	COST OF STRUCTURES	3.2
26.02	MECHANICAL EQUIPMENT	36.7
26.00	TOTAL MHRE COST	39.9

* COSTS FOR THE HTS COMPONENTS (M$).....

|	M$
1 - RECIRCULATING JET ARRAY SYSTEM	0.0
2 - INTERMEDIATE HEAT EXCHANGER	73.9
3 - PRIMARY LOOP PIPING	48.1
4 - PRIMARY COOLANT CLEANUP PLANT	16.7
5 - PRIMARY COOLANT PUMPS • MOTORS	42.2
6 - SECONDARY LOOP PIPING	25.6
7 - STEAM GENERATOR	55.3
8 - SECONDARY COOLANT PUMPS • MOTORS	59.2
9 - SECONDARY COOLANT CLEANUP PLANT	24.2
10 - STEAM SEPARATOR	11.1
11 - WATER LOOP PIPING	0.2
12 - FLASH BOILER ACCUMULATOR	0.0
13 - STEAM SUPERHEATER	38.7
TOTAL HEAT TRANSPORT SYSTEM COST....	395.1

CT Driven HYLIFE-II Plant
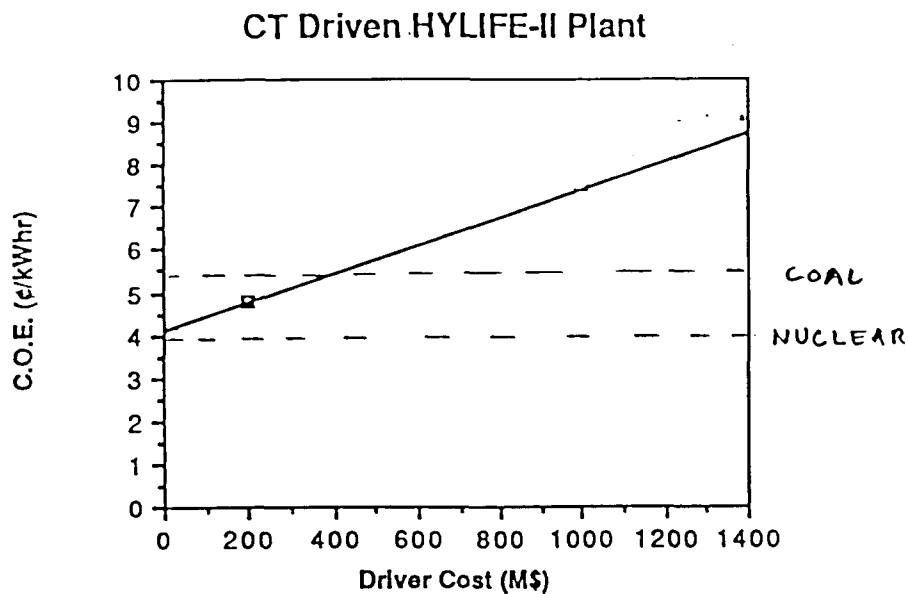
Fig. 6–1. The cost of electricity for the CT ICF reactor is calculated with the SAFIRE code.

For the sake of comparison, (Delene, 1991) estimates the COE in 1990 dollars for nuclear to be 4.3 ¢/kWh for a 1200 MWe unit or 4.5 ¢/kWh for two 600 MW units. The cost of U_3O_8 is assumed to be $110/kg. Delene estimates the COE increases 0.3 ¢/kWh for each $100/kg uranium cost increase. The nuclear cost might eventually increase when uranium becomes scarce and expensive by about 20% to the hybrid limit (hybrid fusion-fusion system where fusion plants produce fissile fuel for fission plants making COE independent of the cost of mined uranium). Added safety features might also increase nuclear's COE. Delene's estimate for coal is 5.8 ¢/kWh for two 600 MWe units. The nuclear and coal costs in Fig. 6–1 were reduced by 8%, to put them in 1988 dollars for an equal comparison.

References

Delene, J. G., (1991), "Update Comparison of Economics of Fusion Reactors With Advanced Fission Reactors," *Fusion Technology*, 19 807.

McCarville, T. J., W. R. Meier, C. F. Carson, and B. B. Glasgow (1987), *SAFIRE: A System Analysis Code for ICF Reactor Economics*, Lawrence Livermore National Laboratory, Livermore, CA, UCRL-15872, Vol. 1.

Bieri, R. L. (1991), "Parametric Cost Analysis of a HYLIFE-II Power Plant," *Fusion Technology* 19, 752-757.

Appendix A. Energy losses in the RACE focusing cone

The Ring Accelerator Code (RAC) is used to evaluate the energy lost in the focusing cone. We depart somewhat from the accelerator dimensions and other parameters discussed elsewhere in this report and base our calculations on a reference compact torus accelerator (CTA) for ICF with parameters given in Table A-I. The accelerated CT ring with, $U_{kinetic}$ = 36 MJ, $U_{magnetic}$ = 0.36 MJ, V = 600 cm/ms, R = 10 cm, D (radial thickness) = 5 cm, and L = 5 cm is assumed to be injected into a focusing cone which converges to R = 1 cm in 250 cm length. At the cone entrance, D = 5. cm and R = 10 cm, and D/R = 0.5 is assumed to remain constant (consistent with RAC assumptions) 240 cm along the cone. For the last 10 cm (240–250 cm) D/R = 0.2 to obtain a D = 0.2 cm annular opening into the flux conserver for preventing reexpansion of the trapped CT back up the accelerator channel. The transition from D/R = 0.5 to 0.2 is achieved in the RAC code by reinitializing the CT ring trajectory calculation with $U_m \sim 1/D$ scaled accordingly and U_k appropriately readjusted.

The electrode energy losses are calculated assuming the focusing cone is made out of Cu. At the high fields (B ≥ 10 MG) produced, the electrode interaction is highly non-linear with vaporization and heating by eddy currents altering the wall resistivity and with strong shock waves launched into the electrodes. In this high energy density region Cu and Flibe are probably similar in effects. For parts of the cone where B £ 10 MG it is possible to add a thin layer of metallic Li.

CT ring energy and losses are summarized in Table A–II for the two sections of the focusing cone, 0 – 240 cm (D/R = 0.5) and 240-250 cm (D/R = 0.2). From the table it is seen that the ring emerges from the focus cone at V = 500 cm/ms with 26. MJ kinetic energy and 4.2 MJ magnetic energy. The largest terms contributing to the loss of kinetic energy are in increasing the magnetic energy by compression during focusing (~4 MJ) and drag on the electrodes (~5 MJ). Most of the drag loss

Table A–I. Reference 100 MJ CTA for ICF.

Accelerator bank energy	100 MJ
Accelerator bank voltage	2.5 MV
Accelerator bank capacitance	30. µfd
Accelerator bank inductance	2.5 µH
Peak accelerator current (at t = 8.0 ms)	5.6 MA
Precompression cone length	3 m
Accelerator section length	27 m
Initial CT ring radius	100 cm
Initial CT ring length	50 cm
Initial CT ring radial thickness	50 cm
Initial CT ring magnetic energy	50 KJ
CT ring mass (10% Xe ions)	2 mgm
Compressed (Accelerated) CT ring radius	10 cm
Compressed CT ring length	10 cm
Compressed CT ring radial thickness	5 cm
Compressed CT ring magnetic energy	0.48 – 0.36 MJ
Accelerated CT ring kinetic energy	36 MJ
Compressed CT ring average field	280 KG
Peak Accelerating field (at center conductor)	150 KG

Table A–II. Reference 100 MJ CTA for ICF.

Axial distance (cm)	0.0	240.0	240.0	250.0	Total
CT ring radius (cm)	10.0	1.04		1.0	
CT ring radial width/radius	0.5	0.5	0.2	0.2	
Kinetic energy (MJ)	36.0	33.0	31.0*	26.0	26.0
Magnetic energy (MJ)	0.36	1.75	4.4*	4.2	4.2
Plasma energy (MJ)	0.002	0.015	0.028*	0.050	0.05
Velocity (cm/µs)	600.0	575.0	550.0*	500.0	500.0
Average magnetic field (MG)	0.28	10.0	42.0	41.0	
Radiation energy loss (MJ)		0.083		0.220	0.3
Resistive decay of magnetic energy (MJ)		0.057		0.2	0.26
Energy loss by drag on electrodes (MJ)		1.2		3.9	5.1

* Magnetic energy increased by $(D/R)_{0\text{-}240}$ / $(D/R)_{240\text{-}250}$, kinetic energy decreased by same amount.

occurs in the final 10 cm long section of the cone where the predominant loss is due to launching strong shock waves in the electrodes by the very high pressure of the 40 MG ring field.

Appendix B. Vapor density limit in the Compact Torus (CT) accelerator

The mass in the CT is typically ~ 10 mg. The mass "swept up" as the CT is accelerated should be much less than 10 mg so that the CT is not slowed down or contaminated. The volume swept out by the 30 m long coaxial annulus of 150 and 75 mm radii is 1.6 m^3. Flibe (Li$_2$BeF$_4$) has a density of 1.25×10^{11}/cm^3 at 475°C which is 15°C above its melting point. The vapor pressure is 0.0013 Pa or 1.0×10^{-5} Torr. At this density there would be 2.0×10^{17} molecules of 26.3 molecular weight giving 8 µg of mass swept up. Thus there would be little slowing down or contamination by the Flibe vapor "colliding" with the accelerated CT.

The rationale for 475°C is as follows. If the accelerator electrodes were held at 475°C, Flibe vapor would condense on the walls and drain to a collection point. At temperatures below 460°C frozen salt would slowly accumulate and the vapor pressure would be even lower and require only periodic defrosting.

By comparison of molecular weights one can see what pressure of other gasses can be tolerated and conclude vacuum requirements can easily be met.

Appendix C. Summary of a past analysis of a compact torus accelerator for ICF

ABSTRACT

We have carried out investigations[15,16] of technical issues associated with using a compact torus (CT) accelerator as a driver for inertial confinement fusion (ICF). In a CT accelerator, a magnetically-confined, torus-shaped plasma is compressed, accelerated and focused by two concentric electrodes. Here, we evaluate an accelerator point design with a capacitor bank energy of 9.2 MJ. Modeled by an O-D code, the system produces a xenon plasma ring with a radius of 0.73 cm, a velocity of 4×10^7 m/s, and a mass of 4.4 µg. The plasma ring energy available for fusion is 3.8 MJ, a 40% driver efficiency. Ablation and magnetic pressures of the point design, due to CT acceleration, are analyzed. Pulsed-power switching limitations and driver cost analysis are also presented. Our studies confirm the feasibility of producing a ring to induce fusion with acceptable gain. However, some uncertainties must be resolved to establish viability.

While several means exist to produce CT's, the method employed here, the co-axial rail gun, was chosen for simplicity and ready adaptation to acceleration and focusing. Here is a typical formation/acceleration sequence:[1] 1) The solenoid capacitor bank is fired at t = 0. These solenoidal magnetic field lines will become the poloidal field of the CT. 2) At $t \cong 1130$ µs, the solenoid capacitor bank is crow-barred. 3) At $t \cong 1180$ µs, the gas valve capacitor bank discharges, opening several fast puff gas valves. Gas fills the gun breech. 4) At $t \cong 1580$ µs, the main gun capacitor bank discharges, ionizing the gas and accelerating the plasma through the toroidal field established in step one. The lines of flux collected by the plasma then become the CT poloidal magnetic field when the lines pinch off. At this point, the CT is formed. 5) At $t \cong 1600$ µs, the accelerating capacitor bank is fired. The current density introduced crossed with the resulting magnetic flux density produces a force that

accelerates the CT. The action is similar to a magnetic piston pushing a sliding short through a co-axial pipe. 6) After acceleration, the CT is focused to the desired radius by entering a conducting cone. The compact torus now moves to interact with the fuel pellet.

The reference accelerator, which replaces the accelerator tip each shot, is likely to survive reactor operation environments (with the possible exception of sputtering). The focusing cone was found in two analysis to ablate and fail by fatigue. Removing/replacing the cone each shot avoids these, potential 'show stoppers'.

CT Properties

In the ring geometry considered in this analysis, the length of the CT is equal to the ring's minor radius. Then, the poloidal and toroidal magnetic fields are approximately equal. The temperature of the compact torus, limited by oxygen and nitrogen impurities, is initially in the 10 to 40 eV range. At formation, the torus may contain 5 kJ of magnetic energy. During acceleration, the magnetic energy decays ohmically with a time constant related by[1]

$$\tau \propto \frac{R^2\, T_e^{1.5}}{Z_{eff}}\ ,$$

(C-1)

where R is the ring radius, T_e is the electron temperature, and Z_{eff} depicts the ionization state. During final focusing the magnetic energy increases in proportion to the inverse of the radius. The ring magnetic energy here can be 75 times the initial value, or more.

The plasma can be described as stable with experimental lifetimes exceeding 1 ms.[2] However, an equilibrium force must consistently be applied to the ring to contain its magnetic fields. Without this stabilizing force, the ring's magnetic fields will expand at the Alfven velocity,

$$v_{Alfen} = B_{CT} \left(\mu_o n_{CT} m_i\right)^{-0.5}\ ,$$

(C-2)

where n_{CT} is the ring ion density, m_i is the ion mass, and μ_0 is the permeability of free space. Since the ring plasma β, the ratio of thermal energy density to magnetic energy density, is small, particles adhere closely to the magnetic field lines and are well contained. Plasma leakage due to local instabilities is small.

The equilibrium force supplied by eddy currents in the electrode walls is removed when the ring leaves the accelerator. Since for current reactor designs, the ring must travel as much as five meters, a propagation scheme must be employed to prevent significant ring expansion before pellet interaction occurs. Two proposals by Meeker are considered.[1] First, a background gas in the reactor chamber would allow the ring to develop a bow-shock wave, providing a restoring force on the ring. However, this scheme would require the ring to have over 100 times more kinetic energy than magnetic energy to prevent excessive energy losses during ring transit. The accelerated ring examined here has a kinetic to magnetic energy ratio of only 10. Therefore, Meeker's suggestion to use lithium jets, or a lithium tube that is replaced after each shot, is more feasible since the ratio of kinetic to magnetic energies is irrelevant in this scheme.

A slow compression-type accelerator with a CT mass of 4.4 μg was designed. Key parameters are listed in Table C-I.

Table C-I. CT accelerator design parameters

CT	Capacitor Bank
Mass ~4.4 μgm (Xe)	Energy ~9.2 MJ
Final radius ~0.73 cm	Capacitance ~718 μF
Final velocity ~4×10^7m/s	Inductance ~500 nH
Kinetic energy ~3.8 MJ	Voltage ~160 kV

Accelerator	System
Length ~12.3 m	Gain ~95
Initial radius ~50 cm	Efficiency ~41%
Current ~5.3 MA	Rep rate ~3 Hz

ELECTRODE RESPONSE TO CT ACCELERATION

An economical lifetime of the CT driver electrodes is paramount to successful reactor operation. The focusing section is exposed to ultra-high magnetic fields and potentially destructive stresses. Electrode lifetime is also shortened by sputtering when discharging at 3 Hz. Electrode design consists of two co-axial tubes of stainless steel. The inner surface of the outer electrode and the outer surface of the inner electrode are copper-plated to a depth of 0.2 cm.

The data collected from RAC output, primarily $B_{CT}(t)$, electrode length and radius, and CT size, are ideal approximations of gun operating conditions. Therefore, results indicate only what may be possible.

Ablation

Surface wall temperatures are first analyzed to determine the location of the onset of melting or vaporization. The only significant contribution to wall heating considered was the ohmic heating caused by the diffusion of the ring magnetic field into the conductor. The conductor surface temperature due to this heating is proportional to the magnetic field squared.

The ring field diffuses on a very short time scale (ns) and to a very small depth (<0.11 cm). Therefore, the flux density in time will be modeled as a step function, where

B (0,t) = 0, for t<0

= B_0, for t>0 .   (C-3)

Magnetic field diffusion into a conductor is synonymous with an influx of energy. The energy increase can be described by Joule's Law. The surface temperature reaches a maximum due to the heat conduction. For copper, this reduces to[3]

$$T_{MAX} = 5 \times 10^5 \frac{B_o^2}{C_v} \ln\left[1 + 990\left(\frac{C_v}{k\sigma}\right)^{1/2}\right] ,$$ (C-4)

where B_0 is expressed in Tesla, and T is expressed in °C. The electrical conductivity (σ), thermal conductivity (k), and specific heat (C_v) were varied with temperature in the calculations.

The accelerator operates in a vacuum. A value of 10^{-6} atmosphere is used based on the vacuum conditions for the Beta II experiment at the Lawrence Livermore National Laboratory.[4] The boiling point of copper (T_B) is 847°C at this pressure.

The surface and skin depth temperatures were calculated. The copper ablates approximately half-way down the final 30 cm focusing cone, where B_0 reaches 150T. The maximum B_0 is 1588T at the cone's tip. The volume of material ablated and vaporized with each firing was estimated to be 0.8 cm^3. This vaporization could prevent the focusing section, over time, from maintaining the small radius rings required for the established fusion gain.

A suggested solution to this problem is to allow liquid lithium to either coat the copper or replace the copper as the conductor over the focusing length. In theory, the lithium would act as an ablator, or sacrificial surface, over the copper.

However, the lithium thickness would have to be at least three times the copper skin depth to carry the same current, since lithium's resistivity is eight times greater than copper's. Maintaining a uniform film would be crucial to ensuring the accelerating flux continues to evenly push the ring. For the accelerator design discussed here, the maximum magnetic field in the horizontal portion of the accelerator is 28T. The cone is replaced each shot since it would be partially destroyed if it were made of steel as the accelerator is. Since the B_{max} <<150T, no ablation is expected in the straight portion of the accelerator.

Magnetic Pressures

The same magnetic flux density that heated the conductor also subjects the gun electrodes to a magnetic stress. If the stresses are too great, the available inner electrode tip cross section may not allow for a sufficient thickness of structural material.

We assume the accelerator electrodes to be infinitely thick conductors because the ratio of the skin depth to the total conductor depth is <<1. We assume the magnetic flux density vector is everywhere parallel to the conductor surface. The resulting pressure is then everywhere normal to the conductor surface. We also assume that the conductor is non-compressible and neglect the potential formation of shock waves that could precede the ring's motion down the gun tube.

Dynamic containment of this magnetic pressure allows the inertia of the electrode to assist in resisting the resultant stress. Dynamic containment is possible because the duration of the pressure pulse (ns) is short compared to the oscillation period of the electrode (μs). The criterion for dynamic containment is[3]

$$\frac{1}{2\mu_0} \int B_0^2 \, dt < \left(\frac{\rho}{E}\right)^{1/2} \sigma_y d \ ,$$

(C-5)

where σ_y is the material yield stress and d is the wall thickness. The density of steel and Young's Modulus are ρ and E, respectively. The time (t) of equation (C-5) is the characteristic diffusion time generated by RAC. Using the surface magnetic induction for both fields (the accelerating B_θ and B_{CT}) at several points, magnetic pressures and required steel thicknesses were calculated.

Stainless steel type 304 is used for the structural wall material, except at the inner electrode focusing cone. When the yield strength of the steel is reduced as the operating temperatures increase toward the electrode tip, a stronger material is required to meet size constraints due to the gun design. When AISI 9840 steel is used, the required wall thickness is less than the maximum allowed dimension, 0.35 cm. However, the steel at the tip cannot exceed an operating temperature of 500°C. Here, active cooling for the inner electrode may be significantly limited.

It is clear that the magnetic pressure, although much greater than the yield stress of steel, can be contained due to the very short exposure time. The focusing section of the accelerator may pose significant heat transfer difficulties due to limited surface area and extreme conductor temperatures. Fatigue failure due to cyclic loading was not considered here.

THERMAL STRESS AND FATIGUE

A temperature difference across the walls of the tubular electrode material induces a thermal hoop stress expressed as:[5]

$$\sigma_{th} = \frac{\sigma_y}{M} \Delta r \frac{q}{A} \quad , \tag{C-6}$$

or

$$\sigma_{th} = \frac{\sigma_y}{M} k \Delta T \quad . \tag{C-7}$$

The value, M, is known as the thermal stress parameter, and is defined as:[6]

$$M = \frac{2(1-v)\sigma_y k}{\alpha E} \tag{C-8}$$

where v is Poisson's ration, α is the coefficient of thermal expansion, and E is Young's Modulus. Large values of M tend to minimize thermal stress.

Equations (C-6) and (C-7) require that $\Delta r \leq 0.2r$, that boundary temperatures are fixed and that there is no internal heat generation. The gun tip dimensions are such that $\Delta r > 0.2r$. At this point the thermal stress is expressed as:

$$\sigma_{\theta_{th}} = \frac{E \Delta T}{2(1-v)}\left(1 + \frac{\Delta r}{3r}\right) , \tag{C-9}$$

or

$$\sigma_{\theta_{th}} = \frac{\sigma_y k}{M}\left(1 + \frac{\Delta r}{3r}\right) \Delta T . \tag{C-10}$$

Boundary temperatures are not fixed, but fluctuate between a minimum and maximum value determined by the rate of heat removal. Maximum temperatures only are used to evaluate the maximum thermal stress. The results are listed in Table C-II.

Table C-II. Summary of possible thermal stresses at the gun tip

x(cm)	1230	
δ(m)	6.77E-6	
d_{cu} (cm)	0.2	
$d_{s.s}$ (cm)	0.335 (510°C)	
ΔT	~50°C	
Δr	0.335 cm	
r	0.93 cm (or 0.01 cm)	
M	4.2×10^3 W/m	
k	20 W/m°C	
σ_{th} (electrode)	Inner	Outer
	$2.9\,\sigma_y$	$0.25\,\sigma_y$

Thermal stress is reduced by three factors: reducing the wall thickness, reducing the heat flux or increasing the thermal stress parameter by choosing a new material. In the case of the CT accelerator, the wall thickness used here represents the minimum thickness that will withstand the magnetic pressure. The wall thickness cannot be reduced. The heat flux is determined by the gun operating conditions and the CT requirements for mass and velocity. As discussed in Chapter three, the CT accelerator specifications chosen represent the maximum mass and maximum radius allowable to generate the fusion reaction. However, a smaller mass and/or radius results in a less efficient accelerator and more energy losses. The most effective way to reduce wall loading is to employ, in this case, two 4.6 MJ drivers or even three 3.1 MJ drivers.

Fatigue of a structural alloy occurs due to the migration of dislocations to grain boundaries under an applied cyclical stress. A complete treatment of fatigue is complicated and relies extensively on empirical data. Conventional stress loading in tests is done at a very slow rate (1–10 Hz). The magnetic pressures of the CT accelerator are applied in less than one millionth of the time loading is done in tests. Empirical equations derived to estimate the number of cycles to failure may be invalid for the cyclic stress of the CT magnetic fields.

The thermal stress is applied over a longer time scale. The number of cycles to failure using the thermal stress only can be expressed as:[7]

$$N_f \approx \left(\frac{\Delta \varepsilon}{\varepsilon_f \bullet 3.5} \right)^{8.33}$$

(C-11)

where $\Delta \varepsilon$ is the ultimate tensile strength to applied stress ratio and ε_f is the fatigue strain parameter. N_f is 0.37 for stainless steel at this temperature.[8] At the gun tip, the total stress is 2.9 σ_y for the thermal stress and 2.7×10^{12} Pa for the magnetic pressure. For a tensile strength of 1.18×10^9 Pa, the number of cycles to failure is

much less than one. This further indicates that equation (C-11) may not be applicable to magnetic pressure applications, since dynamic containment criteria are met. For the thermal stress alone, the number of cycles to failure would be at most about 2 cycles. Since the thermal stress is based on optimistic estimates of the temperature drop across the steel, we can conclude that the gun tip may not withstand two or more discharges before failure.

SPUTTERING

Although ring plasma is generally well confined, ions that do escape cause damage to the electrode walls. Incident ions impart energy to wall lattice atoms through elastic collisions. When the energy transferred exceeds the binding energy of the wall atom, the atom recoils, striking other atoms or leaving the lattice entirely. Energy transfers to atoms not exceeding their binding energy cause heating. The number of atoms displaced per incident ion is the sputtering yield, S.[9] This yield allows calculation of wall erosion rates, a significant detractor from wall lifetime. Significantly, Hartman reports that sputtering or ablated material (with mass equal to that of the CT) does not interfere with ring motion.[10]

Determination of the sputtering yield, in this case for xenon on copper, is dependent on several factors. These are listed in Table C-III.

Table C-III. Factors influencing sputtering yields with specific value ranges for CT driver to be analyzed.

Mass of incident ion	- 131.3 amu
Mass of lattice atom	- 63.5 amu
Anfle of incidence (0° is normal to all)	- 80°–90°
Energy of incident ion	10 eV–1.375 GeV
Wall temperature	150–800°C
Plasma β	0.04–0.36

Many attempts have been made to develop formulas to predict sputtering yields. Models by Sigmund, Thompson and Roth are limited, however, to comparatively small ion energies. In addition, the models do not accurately predict yields for conditions where the incident ion has a much larger mass than the target ion.[11]

The focusing electrode surface vaporizes after approximately one third of the cone length. Sputtering analysis is confined to the solid copper surfaces only. The accelerator is divided into five sections for analysis. The division is based on the relative values of β, ring temperature, wall temperature, and ion kinetic energy. These relative values are listed in Table C-IV.

Table C-IV. Average values for sputtering analysis in each section of the accelerator.

Section	β_{av}	KE_{av}	$T_{i_{av}}$	$T_{wall_{AV}}$	E_i
1	0.04	10 keV	30 keV	0°C	40 keV
2	0.22	0.05 keV	260 keV	150°C	260 keV
3	0.36	375 MeV	0.35 MeV	275°C	375 MeV
4	0.28	1 GeV	0.31 MeV	275°C	1000 MeV
5	0.29	1375 MeV	0.5 MeV	1000°C	1375 MeV

The average plasma β is 0.238.

The total energy of the ion is the most important factor in determining the sputtering yield. The angle of the incident ion is also significant. For angles of incidence between 60° and 70°, the sputtering yield for normal ions can be increased by a factor of three.[12] Data for larger angles (>80°) is generally not available. However, a peak yield seems to occur between 50° and 80°.[13] The sputtered surface temperature affects the overall yield. High temperatures increase the yield in some materials but reduce the yield due to annealing in others. Data indicates silver sputtering yields continue to increase with temperature. Material similarities between copper and silver, common lattice structure and high conductivity suggest similar results are possible for heated copper.

Data for sputtering yields of xenon on copper is generally limited to ion energies less than 100 keV. The sputtering yield is available for the accelerator's first section from appropriate data. A curve representing an approximate fit to this data is used to determine the sputtering yield for the second section. Data further indicates that sputtering of a material can saturate.[14] Therefore, sputtering yields are set at a value of 100 for the remaining three sections. Reported yields have generally not exceeded this value.

The total ion loss rate is determined by the average value of β and the ring transit time in a section. The high estimated yield generally accounts for the large angle of incidence and the elevated wall temperatures. Therefore, an effective sputtering yield is used. Low sputtering estimates use the basic sputtering yield. Results indicating specific sputtering yields and erosion rates are shown in Table C-V. Results indicate that the end of the slow compression section encounters a significantly higher erosion rate. This is expected due to the relatively long time the ring spends there. Engineering solutions to this include: a disposable section, more sputtering resistant copper, or a high conducting protective film that can be periodically reapplied.

Table C-V. Sputtering data and erosion rates in each section.

Section	Ion escaped $(\times 10^{14})$	S_{eff}	S	Erosion High (m/yr)	Low
1	1.6	19	57	1×10^{-6}	3.1×10^{-6}
2	8.73	50	173	6.3×10^{-4}	2.2×10^{-3}
3	1.37	100	390	4.4×10^{-7}	1.7×10^{-6}
4	9.86	100	390	1.5×10^{-7}	5.7×10^{-7}
5	9.63	100	778	1.43×10^{-7}	1.1×10^{-6}

Note: Section Two has a significantly higher erosion rate – between 0.63 and 2.2 mm per year.

CONCLUSION

The temperature profile of the CT accelerator indicates that a significant portion of the electrode copper surface is vaporized with each firing. The quantity ablated is 0.08 cm^3 and represents an average depth of 0.0008 cm.

Magnetic pressures can be contained dynamically in each of three sections analyzed. The average temperature of the steel at the tip of focusing must not exceed 500°C. However, at this temperature, little cross-sectional area remains to actively cool the inner surface to a low temperature. This difficult tradeoff may be solved with liquid metal coolant, a stronger containing material and careful thermal analysis.

The thermal stress is estimated at the inner electrode tip. Results indicate that the stress, based on optimistic estimates, may be fatal to the structure after very few firings.

Erosion rates due to sputtering indicate that the slow compression section of the gun will require frequent replacement or a different design. The erosion in this section is three orders of magnitude greater than any other section.

References

1. D. J. Meeker, "A High Efficiency ICF Driver Employing Magnetically Confined Plasma Rings," *Fusion Technology*, Vol. 9, No. 1, Part 2B (1985).

2. T. R. Jarboe, et al., *Proc. Sixth Symposium Phys. Technol. Compact Toriods*, Princeton Plasma Physics Lab, Princeton, NJ (1984).

3. H. Knoepfel, *Pulsed High Magnetic Fields*, North Holland Publishing Company, Amsterdam (1970).

4. C. W. Hartman and J. H. Hammer, *Acceleration of a Compact Torus Plasma Ring, A proposed Experimental Study*, LL-PROP-191, Lawrence Livermore National Laboratory (1984).

5. T. J. Dolan, *Fusion Research*, Vol. 1, New York: Pergamon Press, p. 684.

6. Dolan, p. 685.

7. Dolan, p. 754.

8. Dolan, p. 756.

9. W. M. Stacey, Jr., *Fusion*, New York: John Wiley and Sons, (1984), p. 88.

10. Hartman and Hammer, *Proposed Study*, p. H-6.

11. P. D. Townsend, J. C. Kelly, and N. E. W. Hartley, *Ion Implantation, Sputtering and Their Applications*, London: Academic Press, (1976), pp. 111-126.

12. M. Kaminsky, *Atomic and Ionic Impact Phenomena on Metal Surfaces*, Berlin, Germany: Academic Press, Inc., (1965), p. 156.

13. Townsend *et al.*, p. 126.

14. Kaminsky, p. 158.

15. M. T. Tobin, "Investigation of a Compact Torus Accelerator as a Driver for Inertial Confinement Fusion," Masters Thesis, UC Berkeley, Nuclear Engineering Department (1985).

16. M. T. Tobin and E. C. Morse, "The Compact Torus Accelerator: A Driver for ICF," *Fusion Technology* 10 679 (1986).